COMPUTATIONAL STUDY ON SEMICONDUCTOR SELF-ASSEMBLY AND MECHANICS OF NANOMEMBRANE

by

Yu Zhang

A dissertation submitted to the faculty of
The University of Utah
in partial fulfillment of the requirements for the degree of

Doctor of Philosophy

Department of Materials Science and Engineering

The University of Utah

August 2011

ABSTRACT

The main objective of this dissertation is to contribute to the understanding of nanomechanics in bilayer Si/Ge thin films and graphene. A set of multiscale modeling and simulations, using finite element analysis (FEA), material point method (MPM) and molecular dynamics (MD) method, have been performed to investigate structural, mechanical and growth properties of several different classes of low-dimensional nanostructures. By using FEA, we find that epitaxially grown Ge quantum dots on both sides of a Si nanoribbon adopt an anticorrelated configuration, in agreement with experiment. In addition, the Ge dots, acting as nanostressors, create a periodic strain field in the Si nanoribbon, which leads to the formation of a new class of single-element strain superlattice as predicted by first-principles electronic structure calculations performed by my collaborators. Also using FEA, we have investigated the morphological instability of strained thin film grown on curved substrates, revealing the physical origin of an anti-phase morphology.

Another accomplishment presented in this dissertation is the understanding of experimentally observed wiggling phenomenon in SiGe nanoribbons released on an SOI substrate. We build a continuum mechanics model to describe the buckling of the strained SiGe nanoribbon and its interaction with the substrate. Our theoretical model provides new insights to understanding the existing experimental results as well as useful guidance

for future experiments, with broad implications in the fabrication of stretchable electronics by strain induced self-assembly.

We also utilized solid mechanics analyses and MD simulations to study the maximum asymmetry in strain induced mechanical instability in graphene, a two-dimensional (2D) crystal with the thinnest possible thickness of only one atomic layer. The continuum mechanics theory shows perfect agreement with the atomistic MD simulation, even down to the scale of a few nanometers.

TABLE OF CONTENTS

LIST OF FIGURES

ACKNOWLEDGMENTS

Though only my name appears on the cover of this dissertation, many people have contributed to its completion. I sincerely thank all the people who have helped me during my 5-year pursuit of a Ph.D. degree.

I would like to express my deepest gratitude to my advisor, Prof. Feng Liu, for his patient guidance, inspiration and criticism during my entire Ph.D. study. Prof. Liu taught me how to think independently, pose questions, and express ideas in a professional way.

I want to specially thank Prof. John Nairn at Oregon State University for his mentorship at the University of Utah and Oregon State University. I really appreciate his generosity for allowing me to use his software NairnFEAMPM.

Dr. Rebecca Brannon is one of the best teachers in my life. She sets high standards in her finite element class, and guides students to meet those standards. With her help, I have a better understanding of the finite element method, as reflected in Chapter 2.

I appreciate the support from members in Dr. Liu's research group, in particular, Hangyao Wang, Decai Yu, Minghuang Huang, and Zhengfei Wang, who have collaborated with me on several research projects. I also thank our departmental administration in helping with me on many logistic issues associated with graduate study, and final support from DOE (Grant No. DE-FG02-03ER46027) for my research assistantship.

Thanks to my PhD committee members, Prof. Miller, Prof. Shetty, Prof. Stringfellow, and Prof. Tiwari, for taking their time to review my dissertation and attend the dissertation defense.

Last but not least, thanks to my immediate family, especially to my parents, Wanjie Zhang and Ruixia Mu. Over the years, they have been constant source of love, patience and support. Special thanks to my wife, Yuan Sun. Without her endless encouragement and love, I could not have finished this dissertation. This dissertation is dedicated to them, and to my beloved daughter, Vivien Zhang.

CHAPTER 1

INTRODUCTION

With the consistent shrinking of feature size in semiconductor devices, strain has been found to be a critical ingredient in the down-scaling of modern devices, which have entered the nanometer scale. Therefore, the study of nanomechanics becomes increasingly important not only as a means to enhance electrical performance through strain engineering, but also with great potential for new application avenues such as in strain induced self-assembly and in stretchable electronics. The focus of my dissertation research is to study nanomechanics of two-dimensional (2D) nanoscale thin films in two materials systems, the SiGe film and graphene (C film); the former is the current choice of electronic material and the latter holds potential as the next generation of electronic material. The most significant result is to show how the properties, especially mechanical properties of nanoscale thin films, will differ from those of macroscopic thick films. Below is the outline of this dissertation.

In Chapter 2, we describe the methodologies used in the multiscale model and simulation, including algorithms of finite element analysis (FEA), material point method (MPM), and molecular dynamics (MD) method.

In Chapter 3, we present results of FEA of self-assembly of Ge quantum dots (QDs) grown on both sides of Si nanoribbons and nanomembranes. We find that due to the

overlapping strain fields and elastic interactions, the Ge QDs on the two sides of the Si nanoribbon/nanomembrane prefer to have an anticorrelated configuration. Furthermore, 3D FEA calculations show that the Ge QDs prefer to nucleate and grow along the <110> crystallographic direction on the (100) surface of thin Si membrane, the most elastic compliant direction of Si nanomembrane. These results agree well with the experimental observations. Using the QD-induced strain fields inside the Si nanoribbon as inputs, first-principles calculations (done by collaborators in our group) further show periodically strain-modulated band gap and carrier mobility in the Si nanoribbons, which form effectively a new class of single-element Si strain superlattice. Also using FEA, we studied the strained thin film growth on curved substrate, and found an antiphase configuration between the film surface undulation and substrate surface undulation. The FAE simulation results agree well with the prediction from continuum mechanics theory.

In Chapter 4, we build a theoretical model based on continuum mechanics and small perturbation theory to explain the wiggling of strained multilayer SiGe nanoribbon and its bonding with the Si substrate. A scaling rule is established between the wiggling period and surface bonding area. The interfacial bonding energy is estimated by fitting the calculated period to the experimental measured ones, and is validated by experimental value estimated from fracture mechanics. Our study provides useful guidance for future fabrication of self-assembly of wiggling structures using semiconductor nanoribbons and nanomembranes.

In Chapter 5, we investigate the strain induced mechanical instability of graphene, comparing the compression induced buckling/rippling instability versus the tension induced fracture, under both uniaxial and biaxial loads. It is found that graphene exhibits

the maximum asymmetry in the compression versus tension induced mechanical instability, because it represents the thinnest possible thin film with only one atomic layer thickness. The continuum mechanics analyses are further confirmed by direct MD simulations. A more complicated form of mechanical instability, such as formation of graphene nanobubbles induced by misfit strain when graphene is grown on a substrate, is also studied using MD. The strain field within the graphene nanobubble will provide critical inputs for studying their electronic properties, which are under way by our collaborators.

CHAPTER 2

METHODOLOGIES

2.1 Finite element method

The finite element method (FEM) is a numerical method in solving structures and continua when the problem is too complicated to be solved analytically [1]. Typical problems that can be solved using this method are stress analysis, heat transfer, fluid flow, and mass transport. First developed in the 1940s in the field of structural engineering, FEM is used to study solution of stress in continuous solids by Hrennikoff and McHenry [2]. With the development of modern computers and efficient algorithms, complicated problems with thousands of equations can be solved in a small amount of time.

The term "finite element" is to distinguish from differential elements in calculus. That is why structure is often modeled as a series of finite elements from discretization. Mathematically speaking, it is a weighted residual method to solve ordinary differential equations (ODE). It solves a total of n equations for n unknowns, formulated in matrix form. The residual is defined as following: to solve an ODE A(u)=f(x), where A is a differential operator and $\hat{u}(x)$ is an approximated solution, residual R(x) is thus defined $R(x) = A(\hat{u}) - f(x)$. It should be noted that residual is different from error, which is a measure of discrepancy between the exact and approximated solution. For example, to

solve an ODE of $y' = e^x$ with boundary condition of y(0)=0, we know the exact solution will be $y' = e^x - 1$. If we choose an approximated solution of $y = 2x$, the residual will be $y = 2 - e^x$, while error will be $y = 2x - (e^x - 1)$.

Since most ODEs do not have analytical solutions due to complicated equations and boundary conditions, finding a best approximated solution is very important. There are several types of weighted residual method (WRM): collocation method, least square method, Galerkin's method, and finite element method [3]. Ritz method, also known as energy method, finds the solution that minimizes the potential of the problem. Ritz method is considered a finite element method to compute the eigenvectors and eigenvalues of a Hamiltonian system in quantum mechanics. Let *R* be the residual of an approximated solution. All the WRMs above use different ways of measuring residuals:

1) Collocation method sets certain values at collocation points, i.e., $R(x_{i\ldots n})=0$;

2) Least square method measures the integration of residuals, i.e., it minimizes |R| in an overall sense in the domain;

3) Galerkin's method converts a continuous differential equation to a discrete problem.

Since finite element is an example of Galerkin's method, Galerkin's method will be explained in detail. For example, if we want to solve a wire problem with governing ODE of $Ty''(x) + w(x) = 0$, where T is the tension in the wire and w(x) is the load applied in y-direction. Galerkin's method starts from obtaining the weak form of ODE: first, multiply ODE by an arbitrary function u(x) and integrate over the domain:

$$\int_0^L [u(x)y''(x) + \frac{1}{T}u(x)w(x)]dx = 0, \text{ for any u(x)} \tag{2.1.1}$$

Eq. (2.1.1) is equivalent of the governing equation in the wire problem. Next, integrate the first term in Eq. (2.1.1) by parts to get:

$$u(x)y'(x)|_0^L - \int_0^L u'(x)y'(x)dx + \int_0^L \frac{1}{T}u(x)w(x)dx = 0 \tag{2.1.2}$$

Rearranging Eq. (2.1.2), we obtain the *weak formulation* of the ODE $Ty''(x) + w(x) = 0$:

$$\int_0^L u'(x)y'(x)dx - \frac{1}{T}\int_0^L u(x)w(x)dx = u(x)y'(x)|_0^L, \ \forall u(x) \text{ (meaning for any u(x))} \tag{2.1.3}$$

The reason Eq. (2.1.3) is called weak formulation is that it has weaker differentiability than the strong form $Ty''(x) + w(x) = 0$. If we use a weight function of $u(x) = \sum_{j=0}^{n} \alpha_j \phi_j(x)$, where α_j are the unknown constants and $\phi_j(x)$ are the basis function. Insert this weight function into Eq. (2.1.3). The equation will become

$$[K]\{A\} = \{f\} \ , \tag{2.1.4}$$

where [K] is the stiffness matrix with $K_{ij} = \int_o^L \phi_i'(x)\phi_j'(x)dx$, {f} is the force matrix with $f_i = \frac{1}{T}\int_0^L \phi_i(x)w(x)dx$, and {A} is the unknown matrix. Since [K] matrix can be calculated using given basis functions and {f} matrix can be obtained by basis function and load function, unknown constants can be solved in Eq. (2.1.4).

By using the weak formulation, the continuity requirements by the original ODE can be weakened. Take wire problem ($Ty''(x) + w(x) = 0$) as an example. The original ODE (in strong formulation) requires the solution be continuous in the first derivative (*y'(x)*), while the weak formulation (Eq. (2.1.3)) only requires y(x) to be continuous. This allows us to find piecewise linear solutions, which is the main advantage of FEM. Therefore, FEM is a unique kind of Galerkin's method, where a simple basis function of

$$\phi_i(x_j) = \delta_{ij}, with \quad \Sigma\phi_i(x) = 1 \tag{2.1.5}$$

which is an interpolation function. Hence, the unknown coefficients A_k can be written as nodal values (displacement) y_k. A great advantage of the piecewise linear basis functions is that they have *compact support*, which means they are nonzero over only a portion of the domain, as can be seen in Eq. (2.1.5). Other basis functions have *global support*, which means nonzero over the whole domain. Compact support allows the integral in the domain to be written as an integral over a set of smaller domains. For example,

$\int_0^L f(x)dx$ can be written as a sum of integrations over *n* discretized elements:

$\sum_{e=1}^{n} \int_{\Omega_e} f(x)dx$, where Ω_e represents the domain of each element.

In conclusion, FEM discretizes the whole domain into smaller domains with piece-wise linear basis functions and uses matrix form $[K]\{A\} = \{f\}$ to solve unknowns in {A} matrix. The more domains discretized, the more accurate the solution is. [K] can be quite large if many domains are discretized, making inverting it difficult and time-consuming. However, by taking advantage of piece-wise linear shape function (or piece-wise polynomial shape function for high-order element), most of the entries in [K] are zero. In addition, [K] is very symmetric and positive definite. Therefore, it can be solved using efficient techniques, such as conjugate gradient method.

In our particular problem of Si/Ge bilayer structure, thermal stress is used. The misfit strain in Si/Ge bilayer structure is due to the misfit strain of the Si and Ge lattices. To interpret the misfit strain in finite element analysis, we consider a composite of two materials with different coefficient of thermal expansion. The governing equation is described as:

$$\{\sigma\} = [E]\{\varepsilon\} + \{\sigma_0\} \tag{2.1.6}$$

where $\{\sigma_0\}$ is the thermal stress. Since the thickness of the materials system in our study is very thin (~nm) comparing to the length and width (~μm-mm), we use plane stress approximation in 2D analysis.

2.2 Material point method

The material point method (MPM) is a particle method in solving computation fluid mechanics and solid mechanics problems. Considered as an extension from particle-in-cell (PIC) in fluid dynamics [4], MPM allows Lagrangian mass points to move through an Eulerian background mesh. In describing motion (kinematics in fluid mechanics), Lagrangian and Eulerian methods use different approaches: Lagrangian method traces trajectories of particles, i.e., at each time step, each particle's position ($u_i(t)$) is recorded; Eulerian method specifies the field, i.e., at each time step, field (such as velocity field $v_i(u_1, u_2, u_3, t)$) at specific position. The two methods are related by differential equation of the trajectory: $\frac{du_i}{dt} = v_i(u_i, t)$. The Eulerian background mesh, which provides a spatial gradient and restores itself at the end of each time step, serves as a computational scratch pad and is convected with material points over time during deformations. [5]

Even though FEM has been successfully developed to solve a wide range of solid mechanics problems, it still has limitations, such as generating complex three-dimensional objects and need for remeshing because of mesh distortion due to large deformations. By taking advantage of Lagrangian and Eulerian method, MPM avoids Eulerian diffusion problem and mesh entanglement problem for fully Lagrangian method when treating large deformation. Furthermore, by using a particle method, MPM is more capable when treating crack propagation, history-dependent problems, and contact problems. However, MPM is more computationally expensive than FEM as it carries both mesh and particle data, and the mesh reinitialization at the end of each time step requires additional computational resource.

The governing equations for solid mechanics are described as [5]:

Equation of motion:

$$M_g a_g = F_{ext,g} - F_{\text{int},g} \tag{2.2.1}$$

Constitutive model between stress and strain:

$$\sigma = T\varepsilon \tag{2.2.2}$$

Relationship between strain rate and velocity gradient:

$$\varepsilon = \frac{1}{2}(\nabla v + (\nabla v)^T) \tag{2.2.3}$$

Different time integration methods are applied in MPM, and the algorithm [5] of MPM with explicit time integration is described here. In solving solid mechanics problems, MPM first discretizes solid body into material points, representing small volumes of material, and then the material points are projected to FEM-styled (Eulerian) grid. By interpolating material point onto the computational grid, the mass matrix M_g is formed. Each material point carries information, such as position x_p, mass m_p, velocity v_p, and external force $F_{ext,p}$. For each grid node, its field information is obtained from particles in the elements containing the grid node. By using the shape function S_{ip} (similar

to the one in FEM), the mass matrix for the *ith* grid node is written as:

$$M_i = \sum_p S_{ip} m_p \tag{2.2.4}$$

The grid node velocity is calculated by interpolating the momentum of surrounding material points of the *ith* node and then weighted with its mass matrix:

$$v_i = \frac{\sum_p S_{ip} m_p v_p}{M_i} \tag{2.2.5}$$

External forces for the *ith* node are interpolated in the same manner:

$$F_{ext,i} = \sum_p S_{ip} F_{ext,p} \tag{2.2.6}$$

The particle velocity gradient is

$$\nabla v_p = \sum_p \nabla S_{ip} v_i \tag{2.2.7}$$

Stress σ_p is then evaluated at each particle by using constitutive model. Next, internal force is calculated as

$$F_{\text{int},i} = \sum_p G_{ip}\sigma_p v_p \tag{2.2.8}$$

Since external and internal forces for each material point have been obtained, for each time step, equation of motion can be solved by using Eq. (2.2.1) to obtain acceleration. The grid velocity is updated:

$$v_g^L = v_g + a_g dt \tag{2.2.9}$$

The information is also updated on each material point by using the shape function S_{ip}:

$$v_p(t+dt) = v_p(t) + \sum_i S_{ip} a_i dt \tag{2.2.10}$$

$$x_p(t+dt) = x_p(t) + \sum_i S_{ip} v_i^L dt \tag{2.2.11}$$

This completes one time step of the calculation. After the end of each time, the deformed grid is reset to its undeformed configuration since positions of grid nodes are never updated.

2.3 Molecular dynamics simulation with empirical potential

Molecular Dynamics (MD), which simulates physical movements of atoms and molecules, has been a great tool in materials science study. [6] This method was

developed in the 1950s [7] and 1960s [8] in the field of theoretical physics. It is a multidisciplinary method involving mathematics, physics and chemistry. As a method of solving many-body problems, MD requires a way to describe how particles (atoms or molecules) interact with each other, namely, potential function, also known as force field in chemistry and biology. The empirical potentials are obtained by fitting against detailed electronic-structure calculations (first-principle calculations) or experimental data of physical properties such as elastic constants, lattice parameters and spectroscopic measurements.

A simple pair potential, such as Lenard-Jones Potential $U(r) = 4\varepsilon\left[\left(\frac{\sigma}{r}\right)^{12} - \left(\frac{\sigma}{r}\right)^{6}\right]$, calculates the sum of energy contributions from pairs of atoms. However, pair potentials cannot always be accurate in describing the force field of many-body problems since dependency between the variables cannot in general be expressed using only pairwise products of the degrees of freedom. Therefore many-body potentials are developed. When treating many-body problems, where three or more particles interact with each other, the potential energy cannot be found by summing pairs of atoms. Being successful in treating carbon, silicon, and germanium, Tersoff potential [9,10], a many-body potential, has been used in my study of graphene mechanical properties. Tersoff potential is a kind of bond order potential, which considers that the strength of a chemical bond depends on the bonding environment, including number of bonds, bond angle and bond length. Tersoff potential describes the interatomic potential with the form of

$$E = \sum_i E_i = \frac{1}{2}\sum_{i \neq j} V_{ij} \tag{2.3.1}$$

$$V_{ij} = f_C(r_{ij})[a_{ij} f_R(r_{ij}) + b_{ij} f_A(r_{ij})] \tag{2.3.2}$$

where E_i and V_{ij} indicate the site energy and bonding energy, respectively. As a function of the atomic distance r_{ij}, f_R, f_A, and f_c represent the repulsive pair potential, attractive pair potential, and cutoff function limiting the range of the potential in order to be computationally efficient. b_{ij} reflects the bond order feature of this potential, while a_{ij} only consists range-limiting terms. The functions above are written in the following detailed forms:

$$f_R(r_{ij}) = A_{ij} \exp(-\lambda_{ij} r_{ij}) \tag{2.3.3}$$

$$f_A(r_{ij}) = -B_{ij} \exp(-\mu_{ij} r_{ij}) \tag{2.3.4}$$

$$f_C(r) = \begin{cases} 1, r_{ij} < R_{ij} \\ 1/2 + 1/2 \cos[\pi(r_{ij} - R_{ij})/(S_{ij} - R_{ij})], R_{ij} < r_{ij} < S_{ij} \\ 0, r_{ij} > S_{ij} \end{cases} \tag{2.3.5}$$

$$\begin{aligned} b_{ij} &= \chi_{ij}(1 + \beta_i^{n_i} \zeta_{ij}^{n_i})^{-1/2n_i}, \\ \zeta_{ij} &= \sum_{k \neq i,j} f_C(r_{ik}) g(\theta_{ijk}) \varpi_{ik}, \\ g(\theta_{ijk}) &= 1 + c_i^2 / d_i^2 - c_i^2 / [d_i^2 + (h_i - \cos\theta_{ijk})^2] \end{aligned} \tag{2.3.6}$$

Subscript *ij* means types of pair atoms, such as Si, Ge and C, and interaction between different atoms are defined as:

$$\lambda_{ij} = (\lambda_i + \lambda_j)/2, \mu_{ij} = (\mu_i + \mu_j)/2,$$
$$A_{ij} = (A_i A_j)^{1/2}, B_{ij} = (B_i B_j)^{1/2}, R_{ij} = (R_i R_j)^{1/2}, S_{ij} = (S_i S_j)^{1/2} \quad (2.3.7)$$

These parameters are defined in [9,10]. Since my study focuses on graphene, parameters of C are used: A=1.3936×10^3 eV, B=3.467×10^3 eV, λ=3.4879 $Å^{-1}$, μ=2.2119 $Å^{-1}$, β=1.5724×10^{-7}, n=7.2751×10^{-1}, c=3.8×10^4, d=4.384, h=-5.7058×10^{-1}, R=1.8 Å, S=2.1 Å.

2.4 References

1. R. D. Cook, D. S. Malkus and M. E. Plesha, *Concepts and Applications of Finite Element Analysis* (John Wiley & Sons, 1989).
2. D. L. Logan, *A First Course in The Finite Element Method* (CL-Engineering, 2010).
3. E. G. Thompson, *An Introduction to The Finite Element Method, Theory, Programming, and Applications* (John Wiley & Sons, 2005)
4. F. H. Harlow, Meth. Comp. Phys. 3, 319 (1963).
5. J. E. Guilkey and J. A. Weiss, Int. J. Numer. Meth. Engng 57, 1323 (2003)
6. M. P. Allen and D. J. Tildesley, *Computer Simulation of Liquids* (Clarendon Press, 1977).
7. B. J. Alder and T. E. Wainwright, J. Chem. Phys. 31, 459 (1959).
8. A. Rahman, Phys Rev 136, 405 (1964).
9. J. Tersoff , Phys. Rev. B 37, 6991 (1988).
10. J. Tersoff, Phys. Rev. B 39, 5566 (1989).

CHAPTER 3

FINITE ELEMENT ANALYSIS OF STRAINED SI SUPERLATTICE WITH DOUBLE SIDED NANOSTRESSOR AND MISFIT STRAIN INDUCED GROWTH INSTABILITY ON CURVED SUBSTRATE

3.1 Introduction

The self-assembled growth process has been widely used for fabricating nanostructures, such as of quantum dots (QDs), which are desirable for applications in nanoelectronic and optoelectronic devices [1-6]. The strain induced self-assembly of QDs is based on the formation of coherent nanoscale structures confined in three spatial directions in strained thin films, via Stranski-Krastanov heteroepitaxial growth mode [7, 8]. The strain induced self-assembly of QDs grown on normal substrate has been studied extensively [9-19]. In order to improve spatial ordering and size uniformity of QDs, several groups have studied self-assembly of QDs grown on patterned substrate [11-13], as well as in multilayer films [20]. In these previous studies, the interaction between the strained islands (i.e., QDs) provides a means of stress relaxation in the film, and the islands which interact with each other are within the same layer and only above the substrate [21].

The mechanical response can be fundamentally different in ultrathin membranes from their bulk counterpart. The growth of QDs, acting as nanostressors, on ultrathin

membrane takes advantage of this interaction and can therefore form small regions of high local strain. Recent experiment [23] shows the Ge QDs can also interact with their counterparts on the other side of the Si substrate when the substrate is thin enough, as can be seen in Fig. 3.1 (a), (b) and (c). This mechanism can also be functional in other strain mediated growth semiconductor systems such as the GaAs/InGaAs system. However, current understanding of the strain interaction based on elastic theory cannot explain such a phenomenon. Our Finite Element analysis gives an explanation to the newly discovered anticorrelation phenomenon.

We have recently found that when the Si membrane is thin enough, it is possible for the Ge QDs, pyramid shaped with {105} facets [9], to interact with Ge QDs on the other side of the Si membrane. Recent experiments have made completely free-standing or partially attached Si nanomembranes, which is then lithographically patterned into free-standing ribbons and deposit Ge/SiGe on both sides of the Si nanoribbons, with a few nanometers thick and tens of micrometers long or longer, detailed experimental procedure is demonstrated in Fig. 3.2. Ritz et al. [23] found that Ge QDs on both sides of the Si nanoribbon surfaces assemble in highly ordered square lattices, which are shifted relative to each other. The rows of QDs in this ordered lattice are aligned with the <100>, which is the elastically “soft” crystallographic directions of Si on both sides of the ribbon, with the Ge QDs on opposing surfaces offset in the <110> direction. We call this phenomenon the anticorrelation effect.

Although the SEM images (Fig. 3.1) have already shown QDs with offset on opposite sides of a membrane, the physical origin is not yet understood. Simulation methods, such as first principle [25] and molecular dynamics [26] have been used to study the Si/Ge

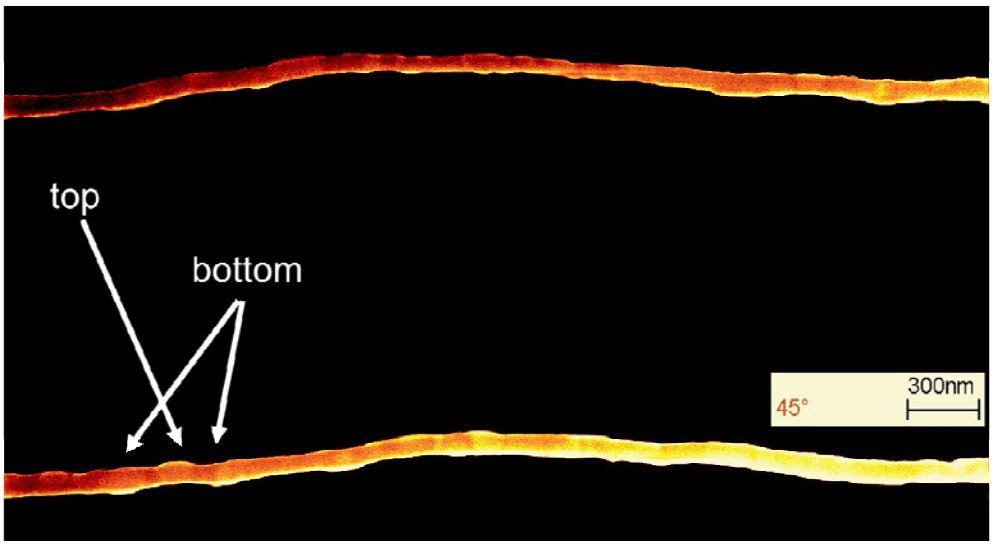

Fig. 3.1 SEM image of double sided Ge QDs on thin Si nanoribbon: (a) side view [23]

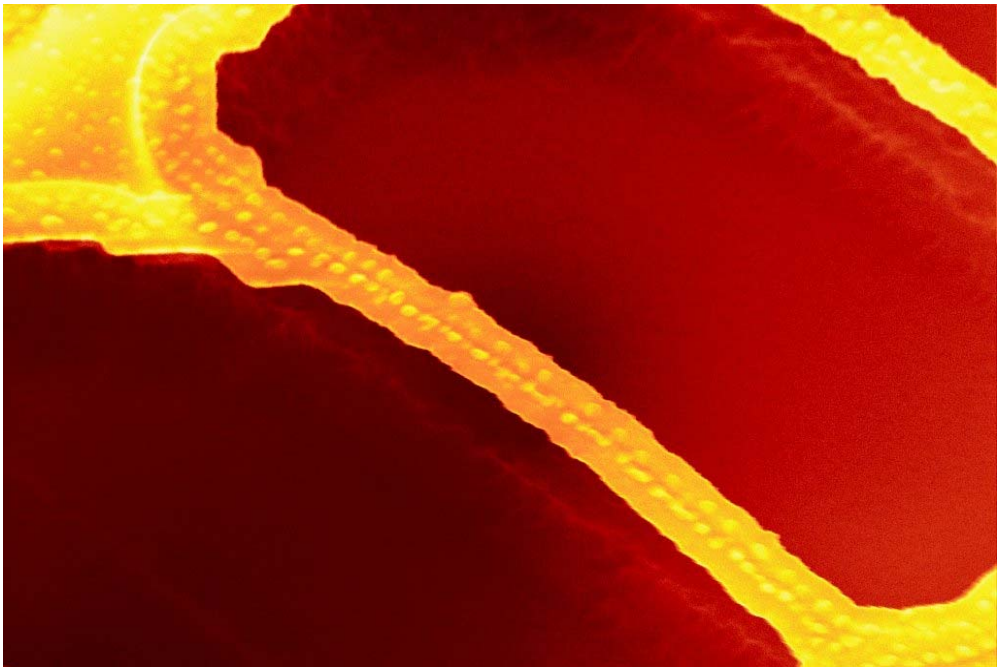

(b)

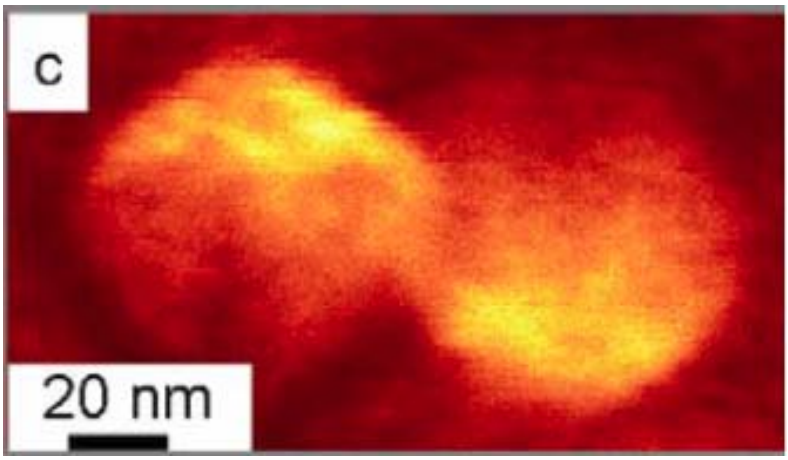

(c)

Fig. 3.1 **(**continued), (b) top view [23], (c) Angled SEM image illustrating contrast between Ge QDs on the top and bottom of a Si membrane. [24]

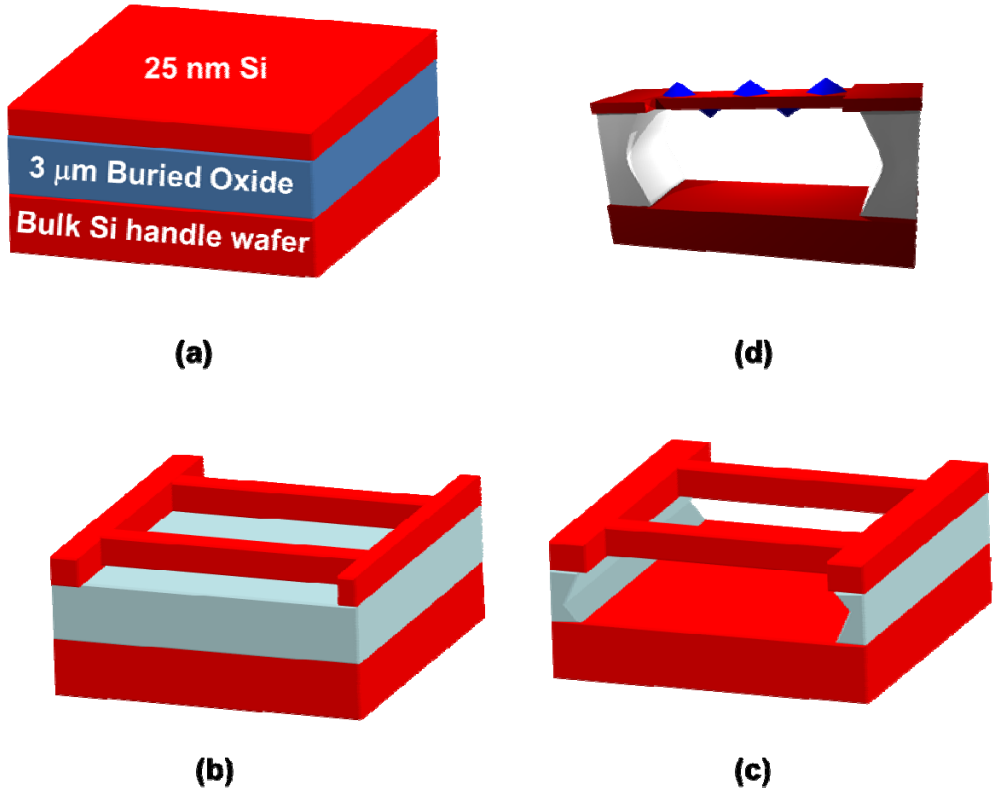

Fig. 3.2 Illustrative model of fabricating Si superlattice with double sided Ge QDs. (a) Initial configuration; (b) After E-beam lithography and reactive ion etching; (c) After Aqueous hydrofluoric acid etching; (d) Double sided Ge QDs growth by chemical vapor deposition. [23]

system, but they are not applicable in studying such an anticorrelation phenomenon due to the size limit of the computation. We introduce the linear elasticity theory and Finite Element Analysis (FEA) in studying the anticorrelation phenomenon [22].

3.2 Two-dimensional FEA model

We perform 2D FEA using NairnFEAMPM software [22, 27]. The FEA uses eight-noded quadrilateral elements and provides 2D plane stress analysis. We also apply periodic strain field boundary condition in our calculation. The two-dimensional FEA model consists of Ge huts, with {105} facets in coherent with the Si (001) substrate, and with height (H) of 8nm and base width (D) of 80nm, and Si membrane, with thickness 25nm. The periodic boundary length (L), which is defined as the distance between Ge huts on both sides of Si membrane, is 140nm. The 2D FEA model is shown in Fig. 3.3. The mechanical properties, including the Young's modulus (E), Poisson's ratio (ν), and the thermal expansion coefficient (α), are the same as previous results [28]. Note that thermal expansion coefficients are arbitrary values. The simulation temperature is chosen to be 10000K to fit the 4% misfit strain.

The feature of periodic boundary condition in FEA is realized by using multipoint constraint, which imposes a relationship between multiple d.o.f (degree of freedom): first, apply a displacement jump between nodes on the left and right boundary,

$$\overrightarrow{u_{Ri}} = \overrightarrow{u_{Li}} + (\Delta u_i, \Delta v_i), \tag{3.1}$$

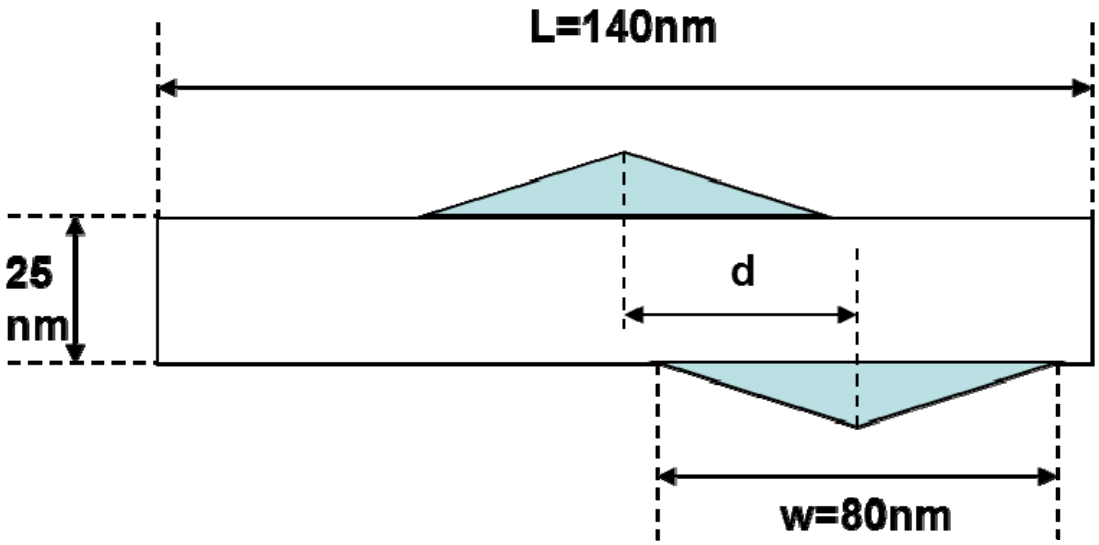

Fig. 3.3 Illustration of the 2D FEA model: with Ge huts (8-nm height and 80-nm wide) on each side of Si substrate (25-nm height). The periodic length for the simulation is 140nm. d indicates the displacement between the Ge huts on top and below the Si substrate within a periodic length**.**

where $\overrightarrow{u_{Li}}$ and $\overrightarrow{u_{Ri}}$ are the displacements of left boundary and right boundary, and u_i, v_i are the constraints in x and y direction. Note: $\varepsilon_{Li} = \frac{\partial \overrightarrow{u_{Li}}}{\partial x}$ and $\varepsilon_{Ri} = \frac{\partial \overrightarrow{u_{Ri}}}{\partial x} = \frac{\partial \overrightarrow{u_{Li}}}{\partial x} + \frac{\partial \Delta u_i}{\partial x}$ according to Eq. (3.1). To make sure $\varepsilon_{Li} = \varepsilon_{Ri}$, which is defined as periodic strain field boundary condition, $\frac{\partial \Delta u_i}{\partial x}$ must be zero. Then apply constraints where the periodic boundary condition is applied in x-direction:

$$v_{Ri} = v_{R1}, u_{Ri} = a + by_i \tag{3.2}$$

Therefore

$$\begin{cases} u_{R1} = a + by_{R1} \\ u_{Rm} = a + by_{Rm} \end{cases} \tag{3.3}$$

where *a* and *b* are solved to be:

$$a = \frac{u_{R1}y_{Rm} - u_{Rm}y_{R1}}{y_{Rm} - y_{R1}}, b = \frac{u_{Rm} - u_{R1}}{y_{Rm} - y_{R1}} \tag{3.4}$$

From the FEA results in Fig. 3.4, we can see the most energetically favorable configuration is the one with anticorrelated mirror configuration. The physical origin for this is that the stress in anticorrelation configuration (d=L/2) is modulated into stress-

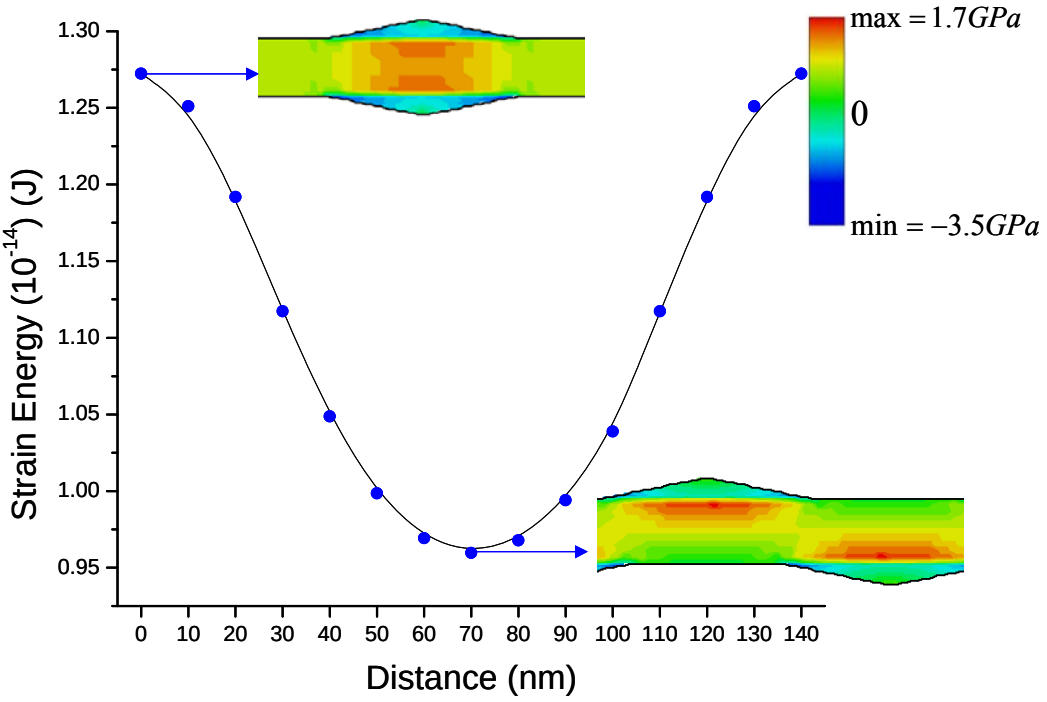

Fig. 3.4 Strain energy versus distance between upper and lower huts in horizontal direction with stress contour plots corresponding to the correlated and anticorrelated configuration.

domain pattern (from the stress contour in Fig. 3.4), while stress is highly concentrated in the correlated structure (d=0, d=L).

Although the most energetically favorable state is where the lower Ge dots have exactly the distance of L/2 from their counterpart on the other side, the energy difference is becoming smaller when the distance is approaching L/2. Will the energy difference be significant in deciding where Ge dots are deposited? Our strain analysis shows that when the Ge coverage is low, there is no significant difference in strain as the distance is increasing, as long as the Ge dots are certain distance apart from the mirrored dots on the other side, seen in Fig. 3.5. From Fig. 3.5, we can also see that the region right beneath Ge QDs is the most compressed region, while the region beneath the corners of Ge QDs is the most stretched region, where Ge QDs prefer to grow due to the fact that Ge has a larger lattice constant than Si.

Because strain can affect electronic properties of semiconductors, this anticorrelated structure with high local strains can have some interesting electronic performances. By incorporating first-principles study [29], we find that the mobility and band gap in the Si superlattice can be altered. Fig. 3.6 and Fig. 3.7 show the hole mobility and band gap contour plot in the 25 nm thick Si thin membrane with double nanostressors (Ge QDs).

3.3 Three-dimensional FEA model

Since Si and Ge are highly anisotropic [30], more accurate results can only be obtained from 3D analysis, even though 2D analysis can provide physical insight to some degree, such as explaining the anticorrelation phenomenon and scaling between dots on two sides of Si nanomembrane.

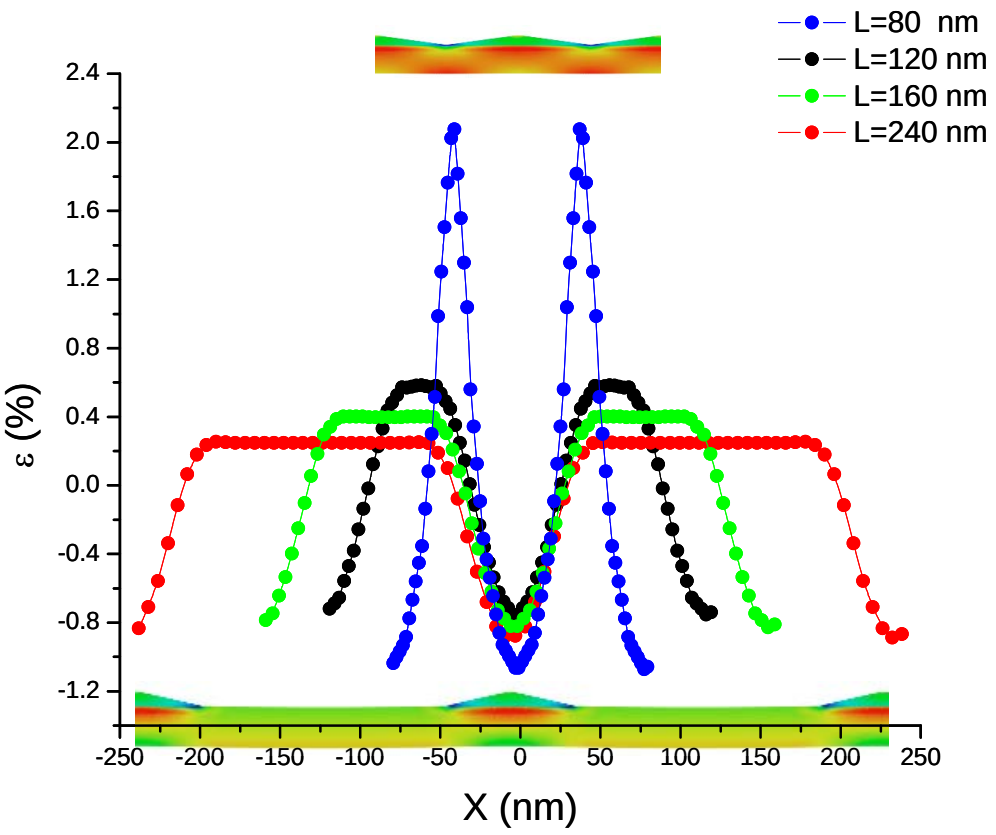

Fig. 3.5 Strain profile on the bottom of Si membrane with different periodic lengths; contour plots are corresponding to the L=80nm (top) and L=240nm (bottom).

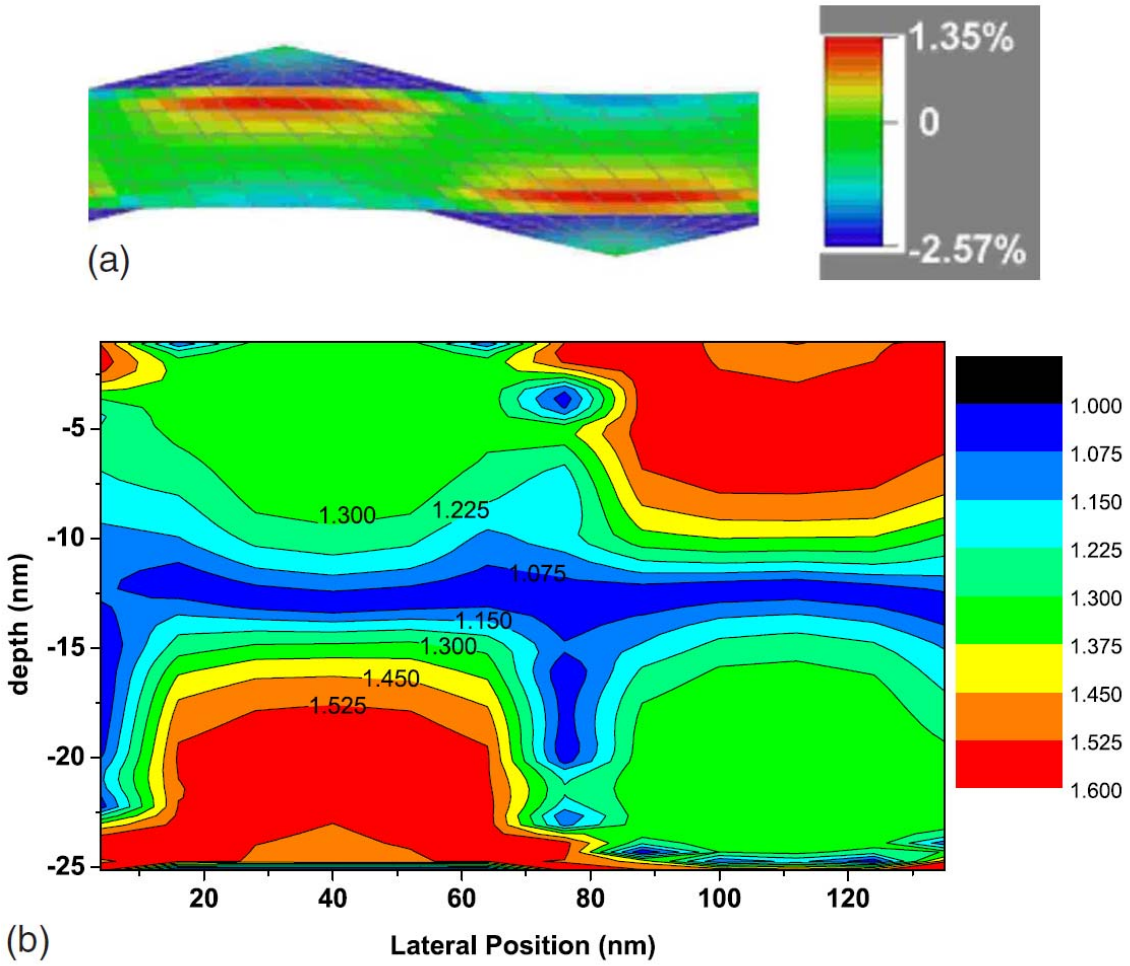

Fig. 3.6 The hole mobility variation in a 25-nm thick Si membrane strained by Ge islands nanostressors on both sides of the membrane. (a) Cross section of the strain distribution in the Si membrane and Ge islands and (b) cross-section modulation map of the hole mobility enhancement in the Si membrane. [29]

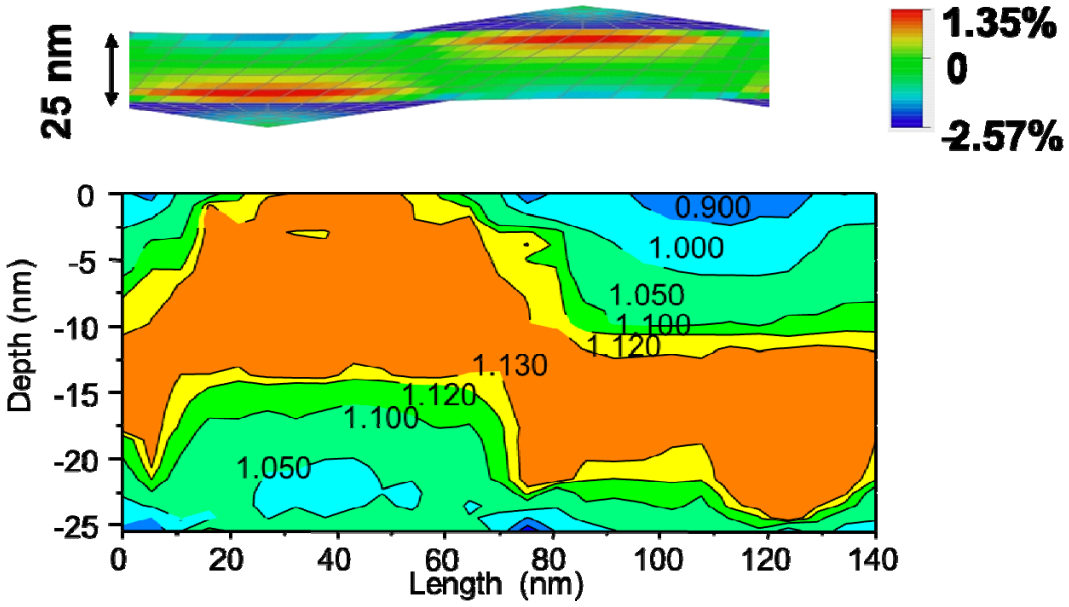

Fig. 3.7 The band gap variation in a 25-nm thick Si membrane strained by Ge islands nanostressors on both sides of the membrane.

Three-dimensional Finite Element Analysis is performed using ANSYS. The geometry is similar to the one in the 2D model, Ge with {105} facets in coherent with the (100) substrate, and base width (D) of 80nm and height (H) of 8nm, aligned along the <100> crystallographic direction on Si membrane, which has thickness of 10nm. We use the anisotropic Si and Ge mechanical properties [30], shown in Eq. (3.5) and (3.6), as well as the symmetry boundary condition in our 3D Finite Element calculation. The schematic three-dimensional model is shown in Fig. 3.8.

$$C_{Si} = 10^{11}\begin{bmatrix} 1.657 & 0.639 & 0.639 & & & \\ 0.639 & 1.657 & 0.639 & & & \\ 0.639 & 0.639 & 1.657 & & & \\ & & & 0.796 & & \\ & & & & 0.796 & \\ & & & & & 0.796 \end{bmatrix}(Pa) \tag{3.5}$$

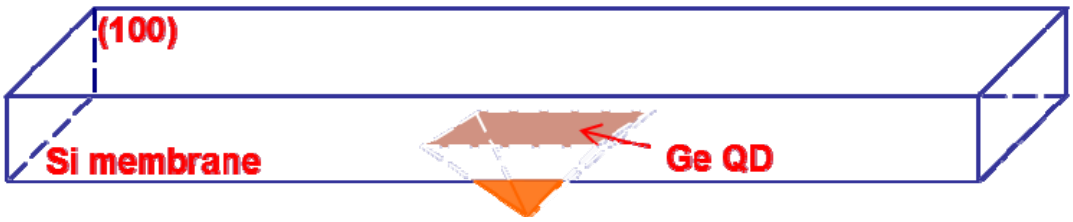

Fig. 3.8 Three-dimensional schematic model for FEA calculation.

$$C_{Ge} = 10^{11} \begin{bmatrix} 1.292 & 0.479 & 0.479 & & & \\ 0.479 & 1.292 & 0.479 & & & \\ 0.479 & 0.479 & 1.292 & & & \\ & & & 0.67 & & \\ & & & & 0.67 & \\ & & & & & 0.67 \end{bmatrix} (Pa) \tag{3.6}$$

Since Si has a 4% less lattice constant (5.43 Å) than Ge (5.65 Å), the more it gets stretched, the more favorable it is for the Ge to deposit and grow on it. The change of differential area can be described in Eq. (3.7) for small strain system:

$$d_S \approx \delta_{Lx}\delta_{Ly}(\varepsilon_x + \varepsilon_y) \tag{3.7}$$

Therefore, we can use $(\varepsilon_x + \varepsilon_y)$ to describe how the area gets stretched, hence to determine the preferred sites for Ge QDs to grow. We plot the $(\varepsilon_x + \varepsilon_y)$ on the bottom of Si membrane (100) surface, over which a Ge hut grows on the other side in Fig. 3.9. As can be seen from Fig. 3.9, the minimum strain (compressed) is where the center of Ge hut in the opposing surface of Si, while the maximum strain (stretched) has an offset in the <110> direction, which means the Ge QDs will be more favorably growing along the <110> direction. Comparing to the 2D FEA results (Fig.3.7), which only gives information on a line (along <100>), the 3D FEA results not only give the 2D information on the bottom of Si membrane, but also predict the preferred direction (<110>) of Ge QD growth, which is consistent with the experimental results [24] and other simulation results [31].

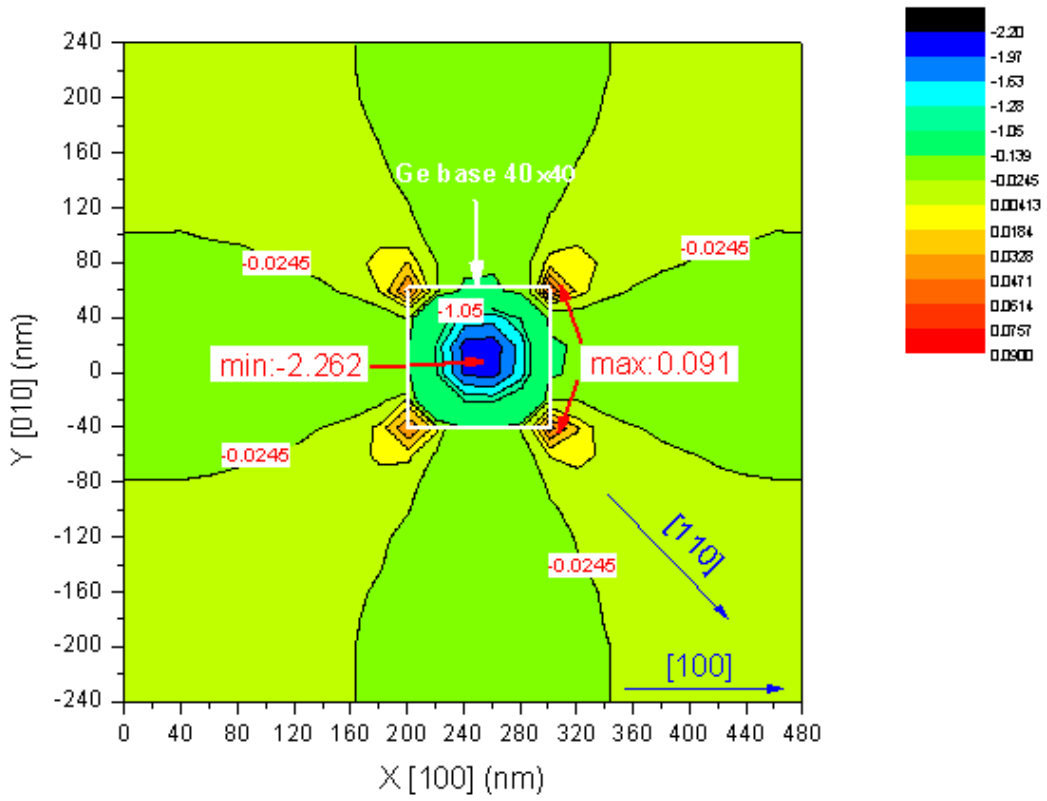

Fig. 3.9 Strain (in percentage) distribution at the bottom of Si nanomembrane with one Ge QD growing at the center on top of the Si nanomembrane.

3.4 Misfit strain induced growth instability on curved substrate

The study of morphological instability of strain thin film has drawn a lot of attention due to scientific importance as well as the potential technological application. As we discussed in the previous section, strain induced self-assembly provides an attractive way of fabricating nanostructures such as quantum dots. However, when grown on a flat substrate, the self-assembled nanostructures are in general not yet uniform enough to be used in practical applications. Recent efforts have been made to combine the strain induced self-assembly with surface patterning in an effort to further improve the size uniformity and spatial ordering of nanostructures [32-36]. Therefore, a fundamental understanding of morphological instability of strained film grown on a patterned or curved substrate is highly desirable.

We first use analytical method [37] to determine the stress distribution in the strained thin film on curved substrate, as shown in the schematic plot in Fig. 3.10. The stress in the x-direction on the film surface can be calculated to the first order as:

$$\sigma_{xx} = \sigma - 2\sigma A_f k_f \sin(k_f x) + 2\sigma A_s k_s e^{-k_s t} \sin(k_s x + \alpha), \qquad (3.8)$$

where the symbols for geometric parameters are shown in Fig. 3.10, and σ is the nominal biaxial stress in the film [37]. The first two terms in Eq. (3.8) are the stresses on a flat substrate, and the third term is the stress due to the curved substrate. The stress in y-direction is negligible since it is much smaller than the stress in x-direction. Note the sign difference of the second and third terms in Eq. (3.8), which can be understood by thinking of the case with a wavy film surface on a flat substrate surface giving rise to the

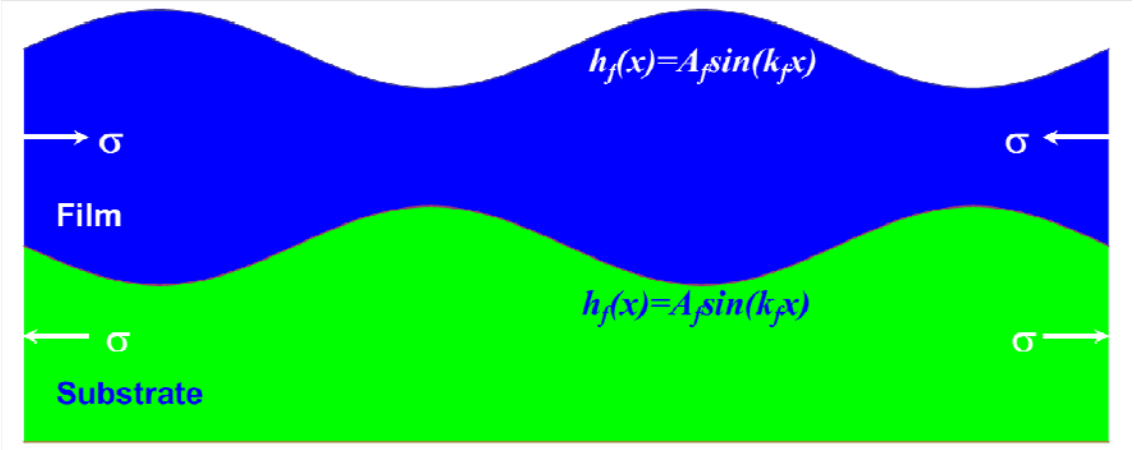

Fig. 3.10 Schematic plot of sinusoidal thin film grown on sinusoidal substrate. [37]

second term versus the case with a flat film surface on a wavy substrate giving rise to the third term. In the former (latter) case, the local film volume is increased (decreased) in the peak region of the film (substrate) surface undulation but decreased (increased) in the valley region so that the normal compressive surface stress is relaxed (enhanced) in the peak region but enhanced (relaxed) in the valley region.

The strain energy density along the top surface along the top surface can be calculated as:

$$w(x) = w_0[1 - 4A_f k_f \sin(k_f x) + 4A_s k_s e^{-k_s t} \sin(k_s x + \alpha), \tag{3.9}$$

where $w_0 = (1-\nu)\sigma^2 / 4E$, ν is the Poisson's ratio and E is the Young's modulus. Strain energy is minimized using variational approach and taking the variation with respect to the film undulation:

$$\frac{\partial U}{\partial A_f} = \int w(x) \sin(k_f x) dx \tag{3.10}$$

Integrating Eq. (3.10) over the whole domain and averaging it to one wave period,

$$\frac{\partial U}{\partial A_f} = -4\pi w_0 A_f - \frac{4\pi w_0 A_s e^{-k_s t}}{m} \frac{k_f k_s}{(k_f{}^2 - k_s{}^2)} \left[\sin(\frac{2m\pi k_s}{k_f} + \alpha) - \sin\alpha \right] \tag{3.11}$$

The second term in Eq. (3.11) will vanish for the commensurate and incommensurate cases [37].

For the commensurate case, where $k_f=k_s=k$, the strain energy variation per wave period can be calculated as:

$$\Delta U = \int_0^{A_f} \frac{\delta U}{\delta A_f} dA_f = -2\pi w_0 [A_f{}^2 - 2A_f A_s e^{-kt} \cos\alpha], \tag{3.12}$$

where the first term indicates the strain relaxation energy on a flat substrate, and the second term reveals the interaction between buried substrate surface and the undulated film surface. Eq. (3.12) shows that for $-\pi/2 < \alpha < \pi/2$, the strain energy on a wavy substrate is higher than the one on the flat substrate, having a maximum energy at $\alpha = 0$, i.e. the in-phase configuration; for $\pi/2 < \alpha < 3\pi/2$, it has a smaller strain energy than the flat substrate case, having a minimum energy at $\alpha = \pi$, i.e., the antiphase configuration.

To confirm the analytical derivation, we perform a finite element calculation using the similar approach discussed in Section 3.2. From Fig. 3.11, we can see that the results based on finite element calculation follows perfectly with the analytical results in Eq. (3.12). The FEA also provides hints on the physical origin of strain energy variation. From the insets in Fig. 3.11, we can see the stress distribution inside the waved film. At the in-phase configuration (the left inset), the stress in the film is rather uniform because of the uniform film thickness, so the film is uniformly stressed without much relaxation. Whereas at the antiphase configuration (the right inset), the stress is highly modulated

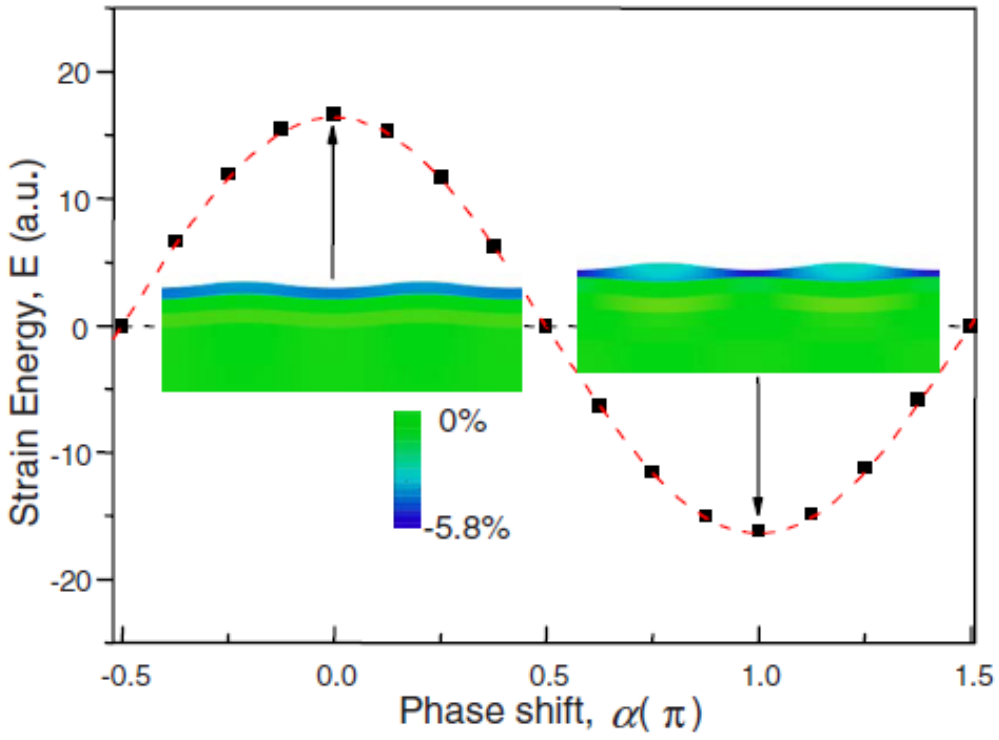

Fig. 3.11 The strain energy E as a function of phase shift obtained from FEA calculations. The energy on a flat substrate is set as the reference energy (E=0). The red dashed line is a fit using a cos function to the calculated data squares. The insets show the stress distributions at the maximum-energy (α=0) and minimum-energy (α=π) configurations, respectively. [37]

into a stress-domain pattern caused by the largest film thickness variation with alternating tensile and compressive domains in the valley region of the substrate (the thick film region) and in the peak region of the substrate (the thin film region), respectively. Consequently, the antiphase configuration has the minimum strain energy through the formation of stress domains as an effective mechanism for strain relaxation [38].

3.5 Summary

In conclusion, we present 2D and 3D Finite Element analysis on the self-assembly of the Ge QDs on both side of the Si nanoribbon and nanomembrane. We demonstrate that Ge QDs adopt an anticorrelated configuration to minimize the strain energy by reducing the repulsive elastic interaction between the QDs mediated through the Si nanoribbon and nanomembrane. Ge QDs prefer to nucleate and grow along the <110> crystallographic direction on one side of the (100) surface of Si nanomembrane, with offset of Ge QDs aligned along the <100> direction on the other side of the Si membrane. FEA shows the physical origin of the anticorrelation phenomenon is due to the strain relaxation by forming stress-domain structure. Similar mechanism applies to the antiphase structure found in the FEA calculation of strained thin film grown on waved substrate.

3.6 References

1. W. G. van der Wiel, S. De Franceschi, J. M. Elzerman, T. Fujisawa, S. Tarucha, and L. P. Kouwenhoven, Rev. Mod. Phys. 75, 1 (2002).

2. T. Lundstrom, W. Schoenfeld, H. Lee and P. M. Petroff, Science 286, 2312 (1999).

3. J. Weis, R. J. Haug, K. v. Klitzing, and K. Ploog, Phys. Rev. Lett. 71, 4019 (1993).

4. R. J. Warburton, C. Schäflein, D. Haft, F. Bickel, A. Lorke, K. Karrai, J. M. Garcia, W. Schoenfeld and P. M. Petroff, Nature 405, 926 (2002).

5. Y. Narukawa, Y. Kawakami, M. Funato, S. Fujita, S. Fujita, and S. Nakamura, Appl. Phys. Lett 70, 981 (1997).

6. R. L. Sellin, Ch. Ribbat, M. Grundmann, N. N. Ledentsov, and D. Bimberg, Appl. Phys. Lett. 78, 1207 (2001).

7. S. Guha, A. Madhukar, and K.C. Rajkumar, Appl. Phys. Lett. 57, 2110 (1990).

8. D. J. Eaglesham and M. Cerullo, Phys. Rev. Lett. 64, 1943 (1990).

9. Y.-W. Mo, D. E. Savage, B. S. Swartzentruber, and M. G. Lagally, Phys. Rev. Lett. 65, 1020 (1990).

10. F. Liu and M. G. Lagally, Surf. Sci. 386, 169 (1997).

11. S. Kiravittaya, A. Rastelli, and O.G. Schmidt, App. Phys. Lett. 87, 243112 (2005).

12. B. Yang, Feng Liu and M.G. Lagally, Phys. Rev. Lett. 92, 025502 (2004).

13. J. L. Gray and R. Hull, J. Appl. Phys. 100, 084312 (2006).

14. F.M. Ross, J. Tersoff, and R.M. Tromp, Phys. Rev. Lett. 80, 984 (1998).

15. A. W. Woll, P. Rugheimer, and M. G. Lagally, Mater. Sci. Eng. B 96, 94 (2002).

16. T. I. Kamins and R. S. Williams, Appl. Phys. Lett. 71, 1201 (1997).

17. H. Lee, J. A. Johnson, M. Y. He, J. S. Speck, and P. M. Petroff, Appl. Phys. Lett. 78, 105 (2001)
18. T. Kitajima, B. Liu, and S. R. Lenoe, Appl. Phys. Lett. 80, 497 (2002).

19. A. Karmous, A. Cuenat, I. Berbezier, S. Atha, and R. Hull, Appl. Phys. Lett. 85, 6401 (2004).

20. M. M. Roberts, L. J. Klein, D. E. Savage, K. A. Slinker, M. Friesen, G. Celler, M. A. Eriksson and M. G. Lagally, Nature Materials 5, 388 (2006).

21. G. Capellini, M. D. Seta, F. Evangelisti, V. A. Zinovyev, G. Vastola, F. Montalenti, and L. Miglio, Phys. Rev. Lett. 96, 106102 (2006).

22. M. Huang, C. S. Ritz, B. Novakovic, D. Yu, Y. Zhang, F. Flack, D. E. Savage, P. G. Evans, I. Knezevic, F. Liu, and M. G. Lagally, ACS nano 3, 721 (2009).

23. C. S. Ritz, American Physical Society March meeting (2007).

24. C. S. Ritz, D. M. Detert, M.M. Kelly, D. Yu, Y. Zhang, M.-H. Huang, F. Flack, D. E. Savage, Z. Cai, P.G. Evans, F. Liu, and M. G. Lagally (unpublished).

25. G. H. Lu, M. Cuma, and F. Liu, Phys. Rev. B. 72, 125415 (2005).

26. J. Zang, M. Huang, and F. Liu, Phys. Rev. Lett. 98, 146102 (2007).

27. JANFEA is a finite element/MPM package developed by Professor John A. Nairn. http://oregonstate.edu/~nairnj/JANFEA/index.html

28. M. Huang, J. A. Nairn, F. Liu, and M .G. Lagally, J. Appl. Phys. 97, 116108 (2005).

29. D. Yu, Y. Zhang, and F. Liu, Phys. Rev. B 78, 245204 (2008).

30. J. Wortman and R. Evans, J. Appl. Phys. 36, 153 (1965).

31. H.-J. Kim-Lee, D. E. Savage, C. S. Ritz, M. G. Lagally, and K. T. Turner, Phys. Rev. Lett. 102, 226103 (2009).

32. G. Jin, J. L. Liu, S. G. Thomas, Y. H. Luo, K. L. Wang, and B. Y. Nguyen, Appl. Phys. Lett. 75, 2752 (1999).

33. T. Kitajima, B. Liu, and S. R. Leone, Appl. Phys. Lett. 80, 497 (2002).

34. Z. Y. Zhong, A. Halilovic, M. Muhlberger, F. Schaffler, and G. Bauer, Appl. Phys. Lett. 82, 445 (2003).

35. B. Yang, F. Liu, and M. G. Lagally, Phys. Rev. Lett. 92, 025502 (2004)

36. L. Bai, J. Tersoff, and F. Liu, Phys. Rev. Lett. 92, 225503 (2004).

37. H. Wang, Y. Zhang, and F. Liu, J. Appl. Phys. 104, 054301 (2008).

38. F. Liu, J. Tersoff, and M. G. Lagally, Phys. Rev. Lett. 80, 1268 (1998).

CHAPTER 4

CONTINUUM MECHANICS STUDY OF SIGE NANOMEMBRANE WITH ITS INTERACTION WITH SUBSTRATE

4.1 Introduction

Electronic devices fabricated on conventional substrate have been widely used in various applications, such as computing, display and photovoltaics. Recently, effort has been devoted to develop stretchable electronics formed on unconventional substrates. Semiconductor materials with good stretchability have drawn much recent attention due to their potential applications in stretchable electronics, especially in large-area electronic displays, sensors and actuators, and optics.[1-11] These structures have been fabricated by vacuum evaporation, photolithographic patterning and mechanical cutting.[1,2,10] For example, stretchable wavy structures in ribbons can be fabricated by bonding patterned ribbons to prestrained elastomeric substrate and then releasing the prestrain.[4-8] Due to strain relaxation in these wavy structures, full stretchability can be realized and fracture limits (~1%) can be exceeded at the circuit level.[4] High performance stretchable electronics can be achieved by integrating such stretchable structures into circuits.

One way to fabricate stretchable electronics is to prestrain semiconductor thin films by using elastomeric substrate, such as polydimethylsiloxane (PDMS), and by releasing the prestrain, wavy structures can be formed. However, this has certain limitations. For

example, the prestrained elastomeric substrate is not reusable and it cannot be directly implanted into the integrated circuits. Furthermore, periodic patterns of the wavy electronics are defined by interfacial activated sites with chemical bonding. Therefore, fabricating self-assembled stretchable structures on electronics-compatible substrate will not only save the additional material as a source of prestraining, but also reduce the effort of defining bonding sites to form desired morphology. It has been shown that self-assembled growth of SiGe nanostructures (such as nanowires) on Si substrate offers such possibility. In this case, the source of prestrain for buckling is from misfit strain between Si and Ge. However, the interaction between the SiGe nanostructure and Si substrate is not fully understood. Therefore, we quantitatively studied the strechability and the effect of surface bonding of SiGe nanoribbon on Si substrate by using continuum mechanics model [12].

4.2 Experimental procedures for fabricating SiGe wiggler

A recent experiment reveals the wiggling phenomenon of SiGe nanoribbon Hall-bar structure bonded to Si substrate [12], shown in the SEM image in Fig. 4.1. The structure is fabricated via the following process: first the sample is prepared by epitaxial growth of sandwich structure consisting of Si, and SiGe thin films, illustrated in Fig. 4.2. The mesa is then defined by lithography and dry etching. The ohmic contacts are created by depositing 10 nm of Au, followed by 4 nm of Sb, then 95 nm of Au. The sample is annealed at 400 °C for 3 minutes and the structure is etched by HF vapor. As can be seen

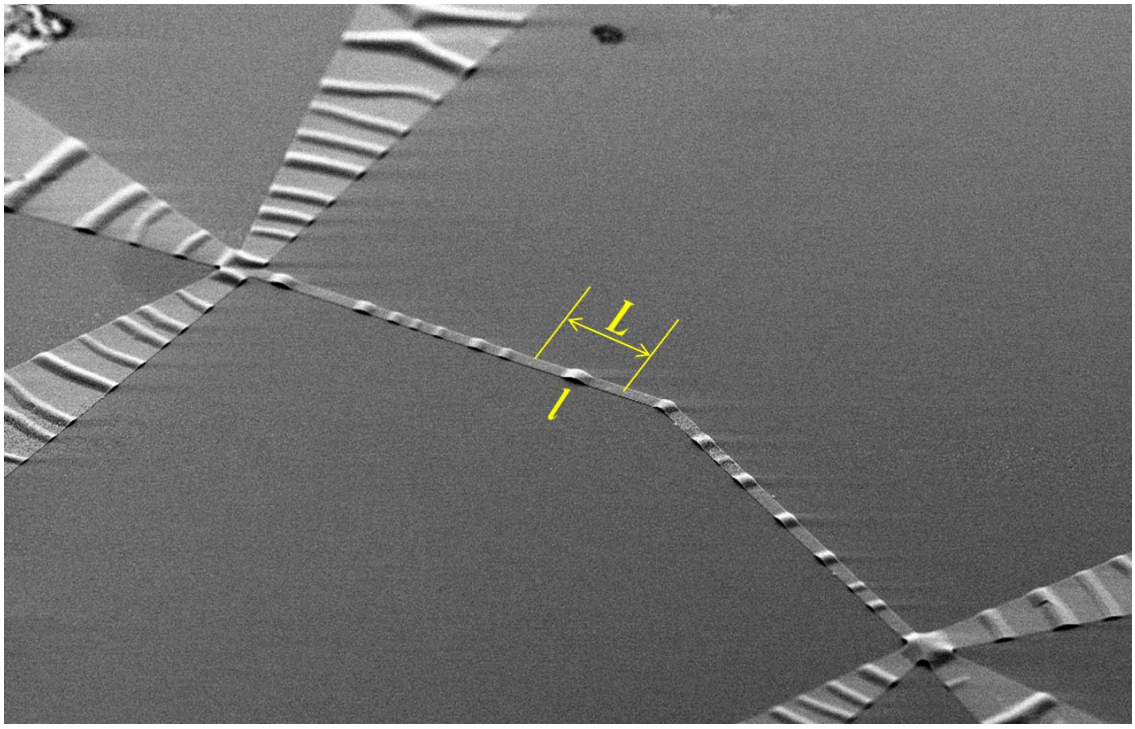

Fig. 4.1 SEM image of wiggled SiGe Hall-bar structure, with undulation width (l) and wavelength (L) indicated. [12]

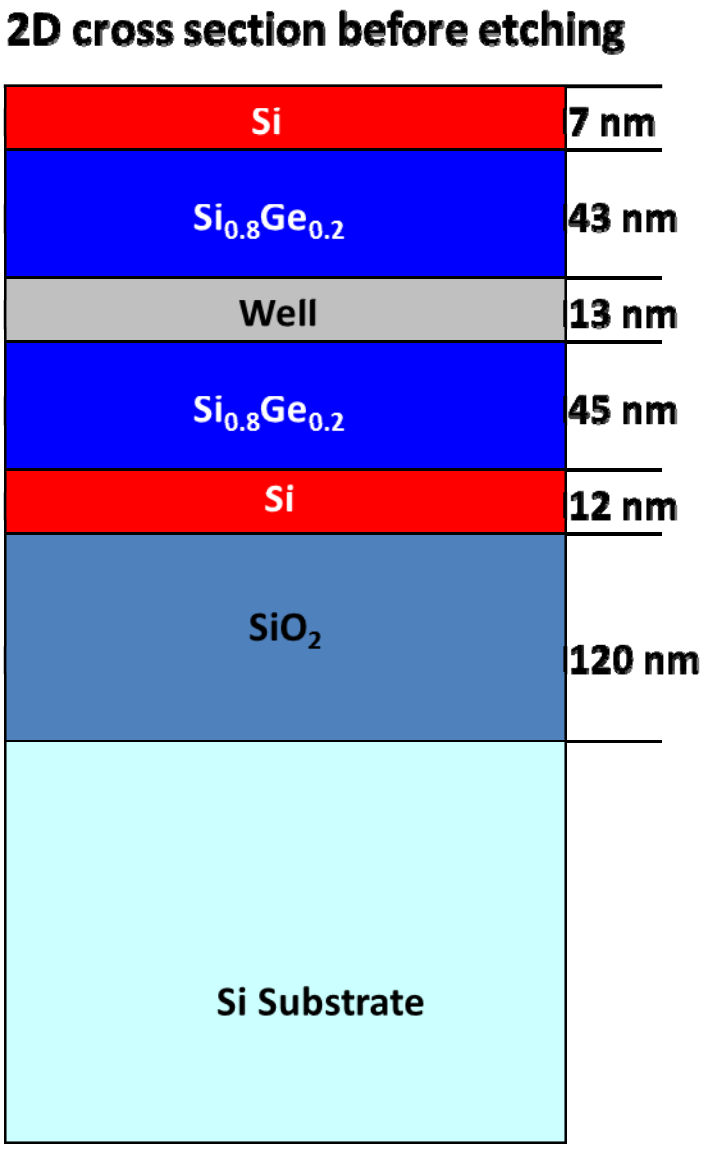

Fig. 4.2 Illustrative model of components and thickness of the sample before etching.

from the fabrication process, no bonding sites are predefined and the wiggler is bonded back to the Si substrate through self-assembling. Further investigation and measurement of the SEM image reveals the periodic pattern of this structure, with some area bonded back to the Si substrate and some area undulated. It can be seen from Fig. 4.3 that undulation *l* varies from 10 μm to 30 μm, and wavelength *L* varies from 20 μm to 200 μm, with the most probable *l* and *L* of 18 μm and 30 μm respectively, which gives the optimal *l/L* ratio to be 0.60. This ratio will later be used as a parameter in our continuum mechanics model.

4.3 Results and discussion

4.3.1 Linear stability analysis of freestanding beam based on continuum mechanics and perturbation theory

To understand the origin of the wiggling phenomenon and determine its characteristic properties, such as periodic pattern of buckled and bonded region and its length scale, we perform a linear stability analysis based on a continuum mechanics beam model and perturbation theory [12]. First, from the construction of the material system, we can conclude there is a compressive residual strain ($-\varepsilon_0$) inside the SiGe nanoribbon. This residual strain is due to lattice mismatch between Si and Ge as the nanoribbon is initially grown and patterned on Si substrate, and its value depends on the material components as shown in Fig. 4.2. Upon releasing the nanoribbon by etching off the SiO_2 sacrificial layer (see the experimental procedure in section 4.2), the beam is expected to undergo a buckling process to relax strain. If the beam were freestanding without bonding to the substrate, the buckling would result in a sinusoidal undulation, as shown in Fig. 4.4 (a). Here we assume the sinusoidal undulation to take the form of

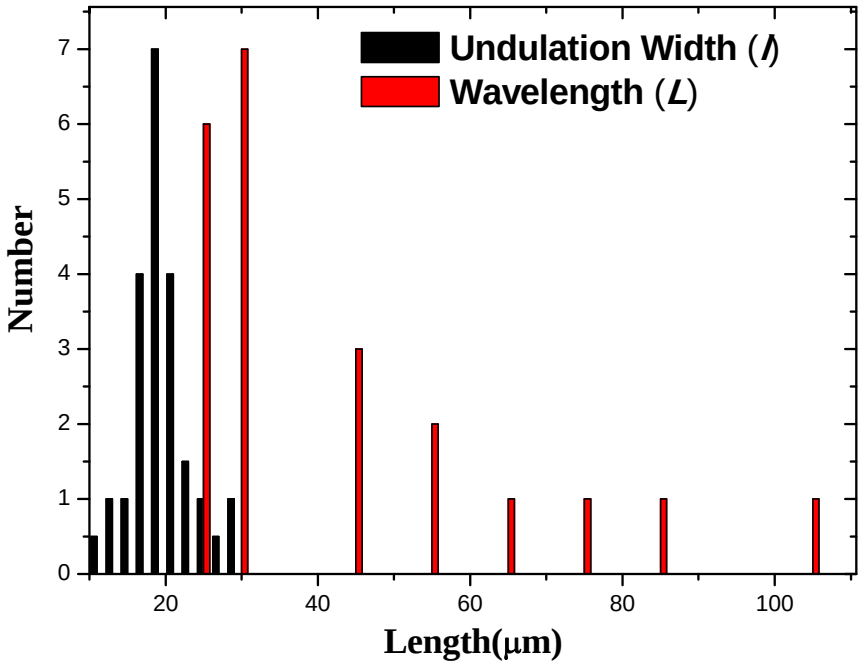

Fig. 4.3 Histogram of undulation l and wavelength L. [12]

$$u(x) = A\cos(2\pi x / L), \tag{4.1}$$

where A and L are the magnitude the and wavelength of the undulation, respectively, as can be seen in Fig. 4.4 (b).

For small perturbation, strain along the wire can be written as (detailed derivation in Section 5.3.2):

$$\varepsilon(x) = \frac{1}{2}\left[\frac{du(x)}{dx}\right]^2 = \frac{2A^2\pi^2(\sin(2\pi x / L))^2}{L^2}. \tag{4.2}$$

In this one-dimensional model, the strain relaxation energy in one wave period of the beam can be calculated as:

$$\Delta U_{Strain} = Wh\int_{-L/2}^{L/2}(-E\varepsilon_0\varepsilon(x) + \frac{1}{2}E\left[\varepsilon(x)\right]^2)dx = Wh(-\frac{\pi^2A^2E\varepsilon_0}{L} + \frac{3\pi^4A^4E}{4L^3}), \tag{4.3}$$

where E, W, and h are elastic modulus, width and thickness of the nanoribbon, respectively. Minimizing ΔU_{Strain} with respect to L, the optimal wavelength is:

$$L_{optimal} = \frac{3}{2}\frac{\pi A}{\sqrt{\varepsilon_0}}, \tag{4.4}$$

which gives the maximum strain relaxation energy of

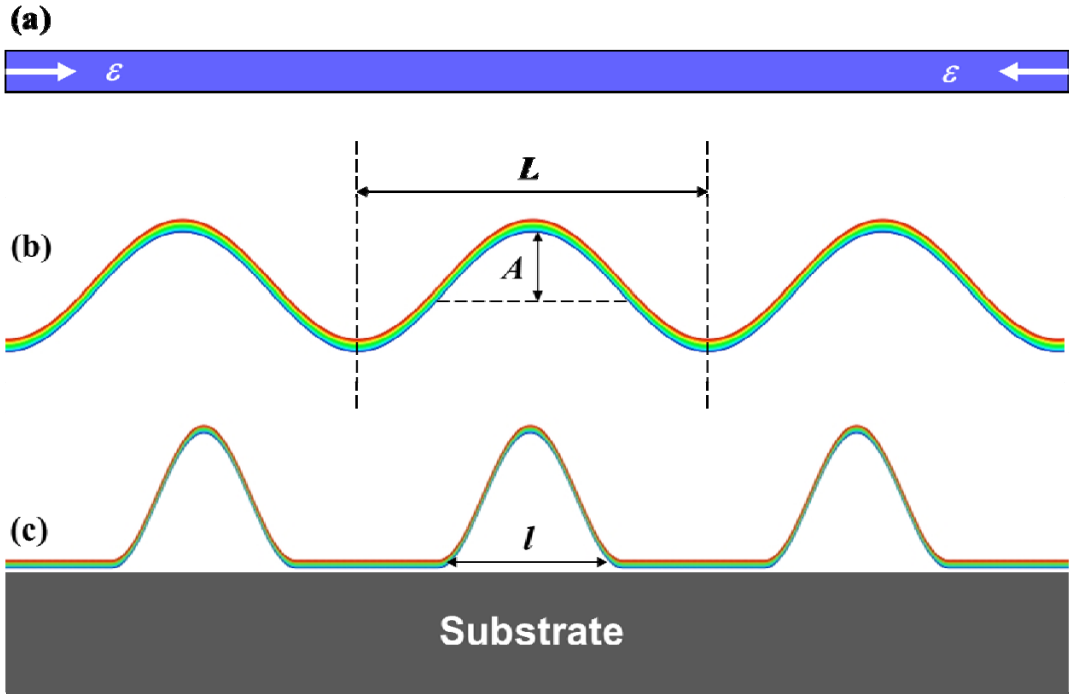

Fig. 4.4 Schematic models: (a) nanoribbon under compressive strain; (b) free standing nanoribbon undulation induced by compressive strain; (c) undulation with interaction of surface bonding. [12]

$$\Delta U_{strain,\max} = -\frac{8}{27} E\varepsilon_0{}^2 V \ , \tag{4.5}$$

where $V=W*L*h$ is the volume of the nanoribbon per period. Comparing to the unrelaxed strain energy of $1/2E\varepsilon_0{}^2V$ without buckling, undulation relaxes the strain energy by 59%. Assuming the undulation to be constant for small perturbation, the larger the residual strain is, the shorter the wavelength will be.

4.3.2 Linear stability analysis of beam bonded on the substrate

If interaction of nanoribbon with substrate is taken into account, one more energy term other strain relaxation energy needs to be considered: interfacial bonding energy. In our model, we consider the interfacial bonding energy to be linearly proportional to the bonding area:

$$E_{bond} = E_b W l' , \tag{4.6}$$

where E_b is defined as the bonding energy coefficient, Wl' is the area that is bonded to the substrate. We can see one that more variable, l', bonded length in the x-direction, is brought into the model. To determine the optimal structure with buckled regions and bonded back regions, we need to obtain the relationship between these variables. For

simplicity, we assume the nanoribbon bonds with substrate at the optimal length L in Eq. (4.4). Upon bonding, the optimal buckled structure in Fig. 4.4 (b), is squeezed into a smaller range of length l, as shown in Fig. 4.4 (c). For simplicity, we also assume the bonded back region to be perfectly flat, and the buckled region has the same amplitude as the freestanding case:

$$u(x) = A\cos(2\pi x / l) + A, x = (-l / 2, l / 2) \tag{4.7}$$

The exact functional form of the wiggler is unknown, but using a different functional form, such as Gaussian function, will not qualitatively change the results.

The next question is whether the bonded back region has a perfect bonding with the substrate, in other words, is it fully relaxed or fully strained? It has been found in experiments that the bonded region can be completely relaxed, completely unrelaxed, or partially relaxed due to interface perfectness [11, 13, 14]. Therefore, we study two extreme cases of bonding, fully relaxed and fully strained.

In the first case, if the bonded region is completely unrelaxed, i.e., fully strained, due to perfect bonding, the change of energy of the whole beam within the original wavelength L is calculated as

$$\Delta U_{Total} = V\left[E\pi^2 A^2\left(-\frac{\varepsilon_0}{lL} + \frac{3\pi^2 A^2}{4l^3 L}\right) - (1 - l / L)(E_b / h)\right]. \tag{4.8}$$

The total energy in this case can be considered as the sum of strain energy, in which strain evenly distributed across the buckled region and bonded-back region, and bonding energy, which is linearly proportional to the area in the flat bonded-back region. Minimizing ΔU_{Total} with respect to l at given L we obtain

$$\frac{l}{L} = \frac{2}{3}\sqrt{-\zeta + \sqrt{(9/2)\zeta + \zeta^2}}\,, \tag{4.9}$$

where we introduce parameter $\zeta = E\varepsilon_0^2 * h/(2E_b)$, the ratio of strain energy over bonding energy per interfacial area between SiGe nanoribbon and Si substrate.

Because considerable strain relaxation is found in the bonded region [13], we investigate the second extreme case, where bonded-back region is considered as completely relaxed, i.e., no strain exists in this region. Since there is no strain relaxation in the bonded region, the residual strain is concentrated in the buckled region:

$$\varepsilon_0^* = (L/l)\varepsilon_0\,. \tag{4.10}$$

Furthermore, the bonding factor E_b can also be different for the two cases, and the bonding factor of the completely relaxed case should be smaller than the completely unrelaxed case:

$$1/\zeta_{relaxed} = \eta/\zeta_{unrelaxed}, 0 \le \eta < 1 \tag{4.11}$$

To determine which of the two cases discussed above is more favorable, we calculate the energy difference between the completely unrelaxed case and the completely relaxed case:

$$\Delta U_{Total,unrelaxed} - \Delta U_{Total,relaxed} = V\frac{E\varepsilon_0^2}{2}(l-L)\left(\frac{(l-8/9L)}{l^2}+\frac{(1-\eta)}{L\zeta_1}\right). \qquad (4.12)$$

Calculating Eq. (4.12) using the experimental data, we obtain if $0\leq\eta<0.82$, the completely unrelaxed case is energetically more stable due to smaller total energy, while the completely relaxed structure is more stable if $0.82\leq\eta\leq1$. Depending on the value of η, which can vary on different parts of the interface due to unevenness, the real case of bonding should be described partially relaxed and partially unrelaxed.

We plot the strain energy, bonding energy, and total energy as a function of (l/L) in Fig. 4.5. As l/L increases, the strain energy decreases in a power law and the bonding energy increases linearly, giving rise to a total energy minimum at the value of (l/L) as given in Eq. (4.9). In Fig. 4.6, we plot the optimal (l/L) as a function of ζ. As ζ approaches zero, i.e., the bonding energy dominating over the strain energy, l goes to zero, so that the whole beam tends to bond with the substrate. As ζ approaches infinity, i.e., the strain energy dominating over the bonding energy, then l goes to L, so that the beam behaves like a freestanding one without substrate. In the experiments (see Fig. 4.1), it was also seen that the period L is larger for wider nanoribbon sections. This might be qualitatively understood with our simple beam-model analysis although it was done with constant width. Effectively, we may consider the wider nanoribbon sections have a

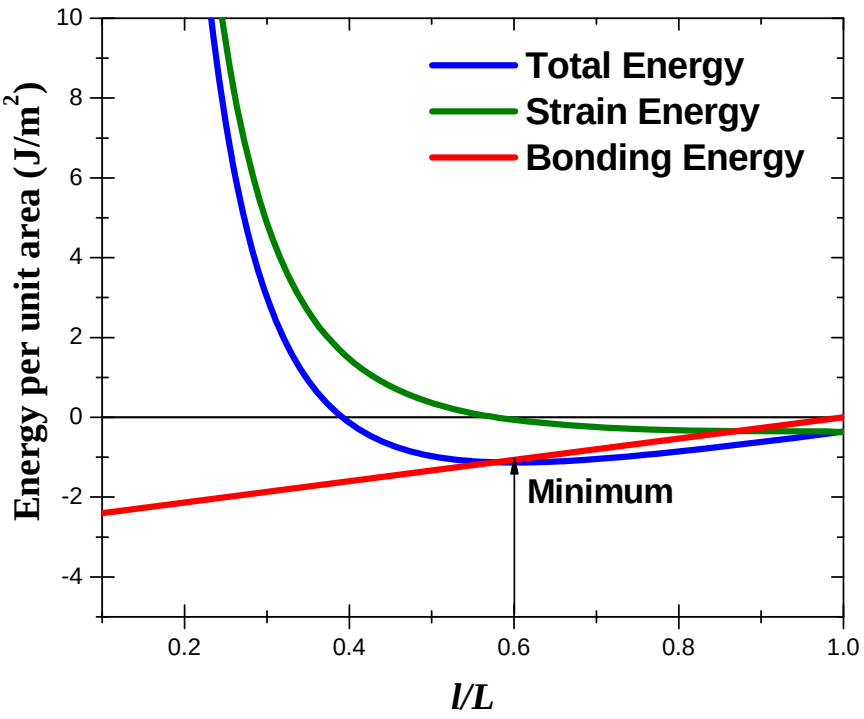

Fig. 4.5 Total energy, strain energy, and surface bonding energy of the wiggled nanoribbon versus dimensionless parameter l/L.

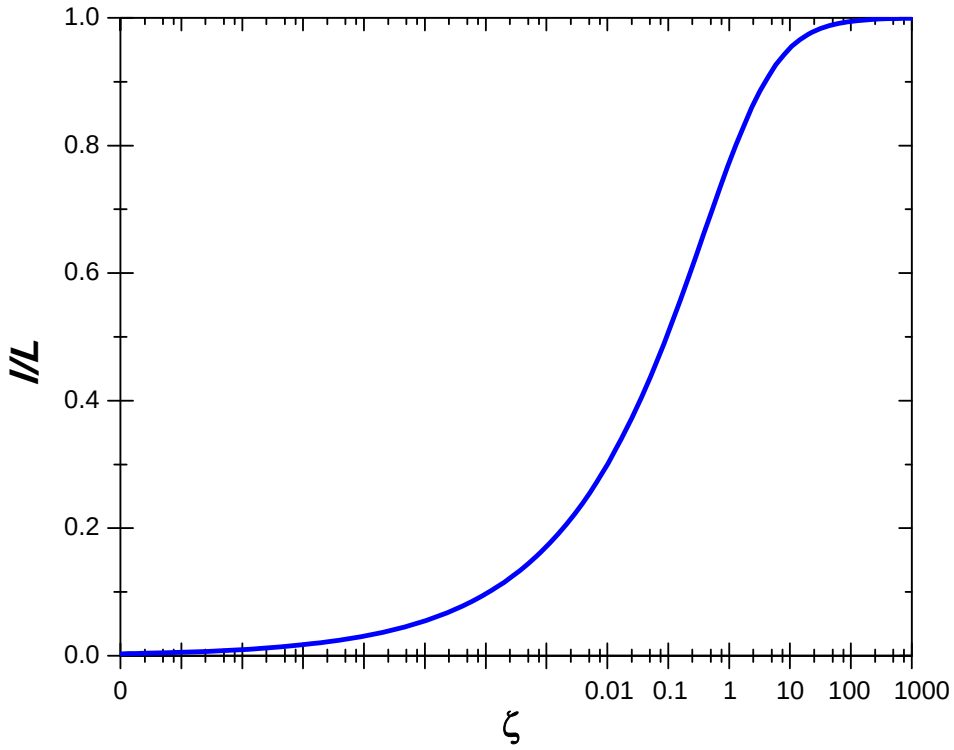

Fig. 4.6 (l/L) as a function of dimensionless parameter ζ.

larger surface bonding energy than the narrower regions, then the parameter ζ will be smaller in the wider regions which will in turn gives a smaller ratio of (l/L) as shown in Fig. 4.6. Now, if we assume the range of the wiggler l to be about the same as shown in Fig. 4.1, then the period of L will be larger in the wider regions of ribbons.

We can conclude that the wiggler dimension (l/L) depends on ratio of the two competing energies: strain energy and bonding energy as shown in Eq. (4.9). Furthermore, from Eq. (4.9), we can estimate the unknown bonding factor E_b by using the experimentally observed dimension (l/L), Young's modulus and thickness of the sample. l/L is found to be 0.6 as discussed in section 4.2, and the ratio (ζ) of strain energy over bonding energy is calculated to 0.23 by using this dimension. The strain energy $E\varepsilon_m^2/2$ of unrelaxed $Si_{0.8}Ge_{0.2}$ per unit volume is 5.07 MPa by using $Si_{0.8}Ge_{0.2}$'s Young's modulus of 158.34 GPa, and residual misfit strain of 0.8% according to Vegard's law. Then, the bonding energy per unit area for (100) plane is $E_b = E\varepsilon_m^2 h/(2\zeta) = 2.67 J/m^2$. Here, E_b can also be interpreted as the interface energy between "bonded" SiGe nanoribbon and Si substrate. The interface energy is the increased energy when two interfaces are created. In our model, the bonding energy, which can be considered as the counterpart of interfacial energy, is the decreased energy when two interfaces are bonded together. That is why in our model, shown in Eq. (4.8), bonding energy always has a negative sign.

In fracture mechanics, Irwin's theory [16] states that the energy in crack growth contains two parts: one is the stored elastic strain energy, which is released as a crack grows and is therefore the thermodynamic driving force for fracture; the other one is the dissipated energy, which includes plastic dissipation and the surface energy and is

therefore the thermodynamic resistance force for fracture. The dissipated energy can be written as:

$$G = 2\gamma + G_p , \tag{4.13}$$

where γ is the surface energy (i.e., interface energy in our previous discussion) and G_p is the plastic dissipation per unit area of crack growth. Since Si is a brittle material, where the plastic dissipation G_p part in Eq. (4.13) can considered as zero, the Griffith energy G (in the unit of J/m^2) can be calculated as 2γ, energy for creating two interfaces. There have been considerable studies of Griffith's energy in literature, both in experimental measurement and in theoretical simulation. Therefore, it provides us a way to validate our model. Our model is a one-dimensional isotropic simplification in Si's (100) surface and the parameters in our model are based on experimental measurement, therefore using experimental data in this particular surface will be ideal to validate this model. In Cook's experimental study, the fracture resistance 2γ is found to be 4.3 J/m^2 along the Si (100) plane, and the corresponding surface energy therefore is 2.15 J/m^2, which is quite close to our estimated value of 2.67 J/m^2. Given the simplicity of our analysis, this level of agreement between our analytical estimation and experimental results is rather satisfactory.

4.4 Summary

In summary, we developed a model based on continuum mechanics to explain the experimentally observed self-assembled wiggling SiGe nanoribbons bonded on a Si

substrate. We believe such wiggling is related to the competition between the strain energy and the interfacial bonding energy. Through continuum linear stability analysis, a scaling rule is established between the wiggling period and surface bonding area. The bonding coefficient is estimated by applying our model to fit the experimentally measured wiggler dimensions and is validated by experimental results in fracture mechanics. Our study provides useful guidance for future fabrication of controllable wiggling structures in self-assembled semiconductor nanoribbons and nanomembranes. Such structures may be used as optical phase gratings or integrated into circuits for high performance stretchable electronics.

4.5 References

1. T. Sekitani, H. Nakajima, H. Maeda, T. Fukushima, T. Aida, K. Hata and T. Someya, Nature Materials 8, 494 (2009).
2. F. Liu, M. G. Lagally and J. Zang, MRS Bulletin 34, 190 (2009).
3. H.O. Jacobs, A. R. Tao, A. Schwartz, D. H. Gracias, and G. M. Whitesides, Science 296, 323 (2002).
4. D.-Y. Khang, H. Jiang, Y. Huang, and J. A. Rogers, Science 311, 208 (2006).
5. T. Sekitani, Y. Noguchi, K. Hata, T. Fukushima, T. Aida, and T. Someya, Science 321, 1468 (2008).
6. C. Harrison, C. M. Stafford, W. Zhang, and A. Karim, Appl. Phys. Lett. 85, 4016 (2004).
7. Y. Sun, W. M. Choi, H. Jiang, Y. Y. Huang and J. A. Rogers, Nature Nanotechnology 1, 201(2006).
8. W. M. Choi, J. Song, D.-Y. Khang, H. Jiang, and J. A. Rogers, Nano Lett 7, 1655 (2007).
9. H. Jiang, Y. Sun, J. A. Rogers, and Y. Huang, Appl. Phys. Lett. 90, 133119 (2007).

10. M. Huang, C. Boone, M. Roberts, D. E. Savage, M. G. Lagally, N. Shaji, H. Qin, R. Blick, J. A. Nairn, and F. Liu, Adv. Mater. 17, 2860 (2005).

11. Y. Mei, D. J. Thurmer, F. Cavallo, S. Kiravittaya, and O. G. Schmidt, Adv. Mater. 19, 2124 (2007)

12. Y. Zhang, M. Yu, D. E. Savage, M. G. Lagally, R. H. Blick, and F. Liu, Appl. Phys. Lett. 96, 111904 (2010)

13. Y. Mei, S. Kiravittaya, M. Benyoucef, D. J. Thurmer, T. Zander, C. Deneke, F. Cavallo, A. Rastelli, and O. G. Schmidt, Nano Letters 7, 1676 (2007)

14. A. Malachias, Y. Mei, R. K. Annabattula, C. Deneke, P. R. Onck, and O. G. Schmidt, ACS Nano 2, 1715 (2008)

15. J. J. Wortman and R. A. Evans, J. Appl. Phys. 36, 153 (1965).

16. G. Irwin, Journal of Applied Mechanics 24, 361 (1957).

17. R. F. Cook, J. Mat. Sci. 41, 841 (2006).

CHAPTER 5

MAXIMUM ASYMMETRY IN STRAIN INDUCED MECHANICAL INSTABILITY OF GRAPHENE: COMPRESSION VERSUS TENSION

5.1 Introduction

Graphene, a perfect 2D crystal with single-layer C atoms that are sp^2 bonded in a honeycomb lattice, has attracted great interest due to its extraordinary mechanical properties [1-3] and promising electronic properties [4]. Even though previously considered to be thermodynamically unstable, monolayer graphene was first discovered by micromechanical cleavage of bulk graphite [5-7]. Other approaches of fabricating multilayer or single-layer graphene, such as chemical vapor deposition and thermal decomposition, are also developed. Graphene patterns, such as graphene nanoribbons (GNR), can be defined by photolithography [8] and chemical treatment [9]. The concept of strain engineering has been proposed to change the electrical properties of graphene and graphene nanopatterns [10], suggesting the all-graphene electronics a future possibility.

Strain has been demonstrated to modulate the electronic properties of armchair GNRs [11-14], magnetic properties of graphene [15] and mobility of graphene. In modifying

band gap of GNRs, a periodic dependence of gap on strain is shown, and the effect of strain on band gap is independent of the sign of strain. However, these theoretical studies are based on the assumption that the flat graphene and GNRs remain stable under the applied strain. Such an assumption can be rather unrealistic, as indicated by the recent experiments [16-17] which showed rippling phenomenon of graphene as a result of thermal induced strain. Since the out-of-plane undulation may make the flat-graphene strain theories invalid, it is important to understand the mechanical instability of graphene against out-of-plane undulation induced by strain, especially the role played by the sign of strain, compression versus tension.

We may ask the general question of how the mechanical instability of a thin film will be dependent on the sign of strain, i.e., compression versus tension. We will first answer this question analytically. Tension will eventually cause the film to break, creating two fracture surfaces. The amount of strain energy should exceed the energy of the two surfaces for fracture to happen, i.e., $1/2A*L*E*(\varepsilon_{cr}^{t})^2 \geq 2A*\gamma$. Therefore, the critical tensional strain for fracture is ($\sim 2\sqrt{\gamma / EL}$), which does not depend on the film thickness. In contrast, compression may cause two types of instability: fracture and buckling. For fracture, the critical compressive strain is comparable to the critical tensional strain since both create two fracture surfaces. For buckling, however, it is quite different. The buckling occurs due to a competition between bending energy of $½*B*\kappa^2*A$ and stretching energy of $½*E*t*\varepsilon_{cr}^{c}*y^2*A$, and because $B \sim t^3$, the critical compressive strain for buckling is $\varepsilon_{cr}^{c} \sim t^2$, which shows a strong dependence on the film thickness. This implies a high asymmetry of strain induced instability in compression versus tensile, as the film thickness is reduced. Fig. 5.1 illustrates such asymmetry of strain induced

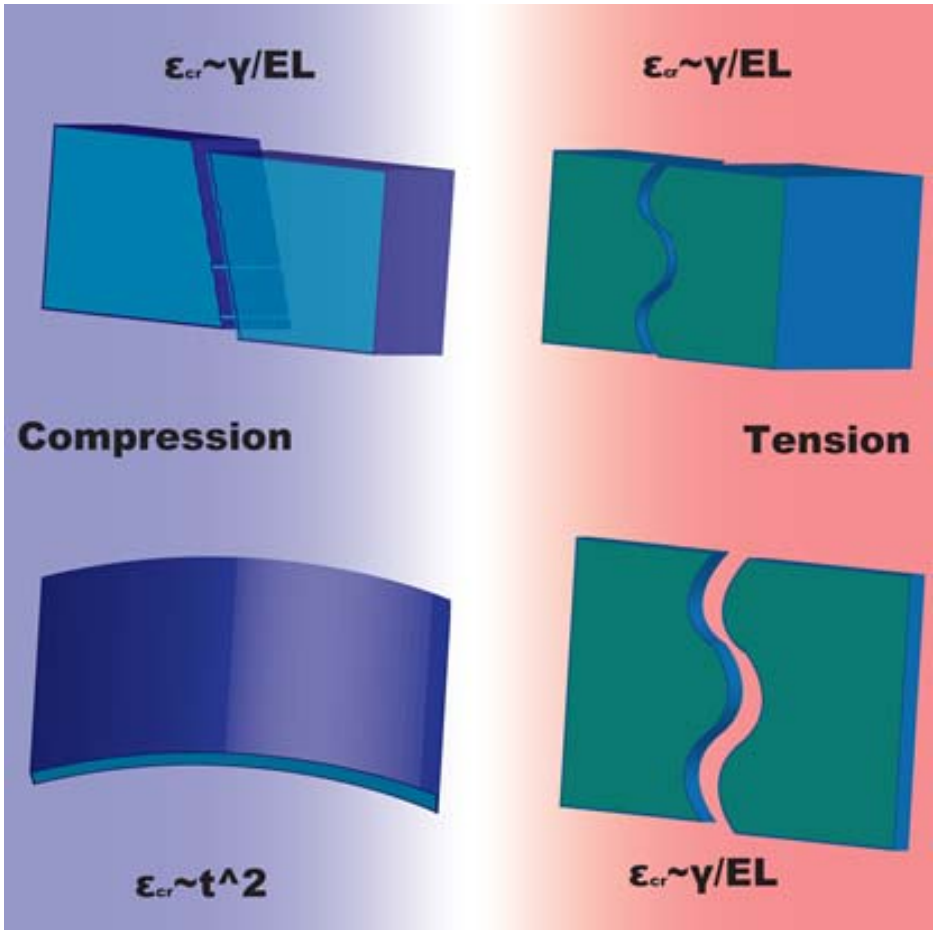

Fig. 5.1 Demonstration of asymmetry of strain induced instability for thick (top) and thin (bottom) films.

instability and its dependence on the film thickness. If the film is thick, towards the bulk limit, then the critical strain is the same for both compression and tension, which is defined solely by the thin film surface energy. If the film is thin, under compression it will buckle first before fracturing, and then the critical strain for the two instability modes can differ significantly, depending on the film thickness.

5.2 Derivation of the strain energy of undulated film

In this section, we present a detailed derivation of strain energy for a 1D beam and 2D film (plate) under undulation. First, let's look at a simple 1D beam problem with small perturbation, as illustrated in Fig. 5.2.

In Fig. 5.2, the vector connecting two points next to each other changes from *dx* to *dl* due to deformation. If we assume the in-plane displacement along x to be zero and consider only the out-of-plane displacement of ζ(x), then we have $dl = \sqrt{dx^2 + dz^2} = \sqrt{1+\left[\zeta'(x)\right]^2}\,dx \approx \left(1+1/2\left[\zeta'(x)\right]^2\right)dx$ for small perturbation. Defining strain as $\varepsilon_{xx} = (dl - dx)/dx$, the strain along the beam (x-direction) is simply

$$\varepsilon_{xx} = 1/2\left[\zeta'(x)\right]^2 \tag{5.1}$$

Alternatively, in Landau's theory [18], strain is generally defined as

$$\varepsilon_{ik} = 1/2\left[\partial u_i/\partial x_k + \partial u_k/\partial x_i + \partial u_l/\partial x_i \bullet \partial u_l/\partial x_k\right], \tag{5.2}$$

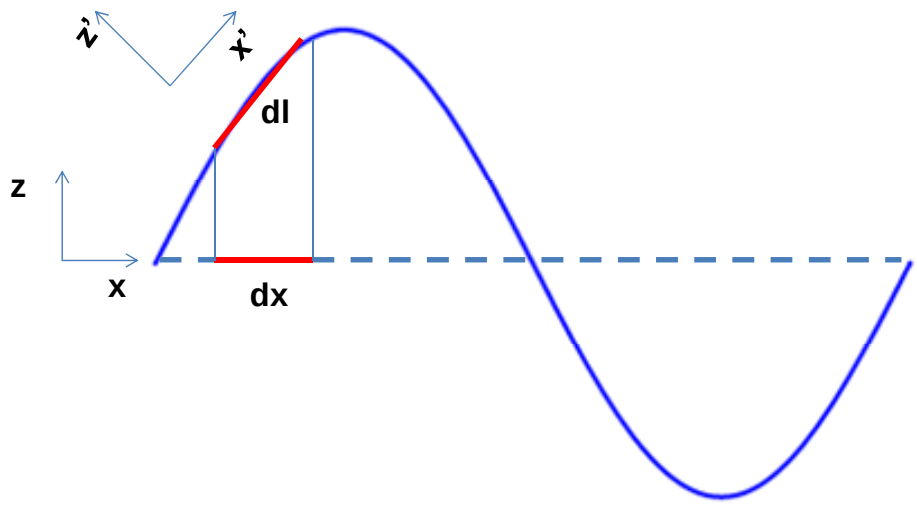

Fig. 5.2 One-dimensional wire problem with local coordinate systems

where the first two terms result from the in-plane displacements and the third term from the out-of-plane displacements. For ε_{xx}, we take $u_i=u_x$, $u_k=u_x$, $u_l=u_z=\zeta(x)$, $x_k=x$ and $x_i=x$, Eq. (5.2) becomes

$$\varepsilon_{xx} = 1/2\left[2\partial u_x / \partial x + \left[\zeta'(x)\right]^2 \right] \tag{5.3}$$

Considering the out-of-plane displacement only, i.e., $u_x=0$, Eq.(5.3) will give the same expression as Eq.(5.1).

Next, we consider the 2D plate (film) problem. If thickness of the film in the z-direction is considered, there will be strain variation along the thickness direction, as shown in Fig. 5.3, which can be determined by analyzing curvature of the film. It is easy to see $dl = (R-z)d\theta = dx - z/R \bullet dx$, which gives

$$\varepsilon_{xx} = -z/R = -\kappa z = -z\partial^2 z / \partial x^2 , \tag{5.4}$$

where R, κ and z are radius, curvature and distance to the neutral axis, respectively.

In the above, it is assumed to have only uniaxial stress, or pure bending, where there are no transverse stresses, i.e., $\sigma_{zz}=0$, $\sigma_{xz}=0$, $\varepsilon_{zz}=-\upsilon\varepsilon_{xx}$, $\varepsilon_{xz}=0$. In other words, warping due to shear deformation is not considered.

To simplify a 3D problem into a 2D model, there are two approximations: plane stress and plane strain. We may adopt Landau's theory [18] considering bending

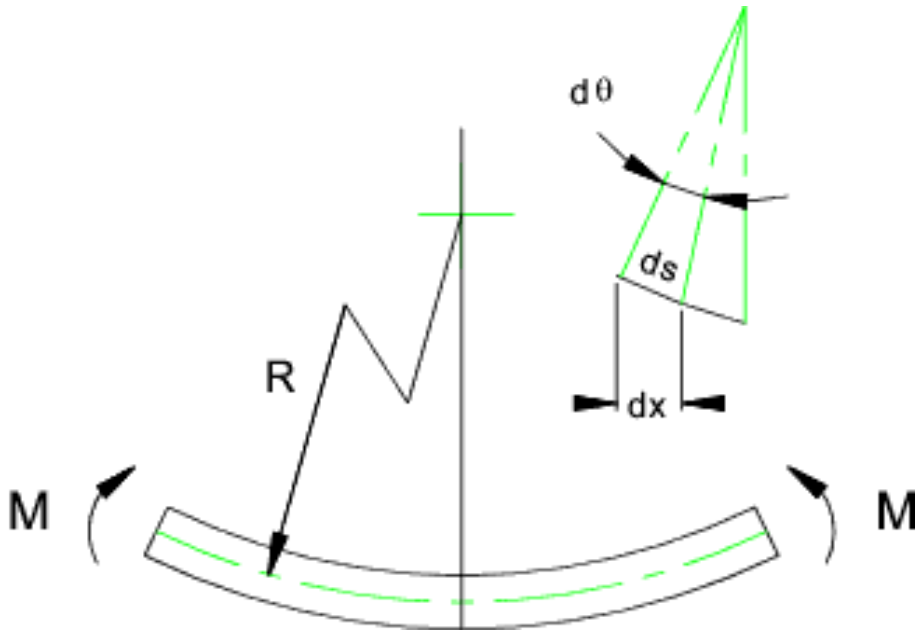

Fig. 5.3 Two-dimensional beam bending

of thin plate to be a *plane stress* problem, which is defined as when thickness *h* (along z)<<*a* (dimension of x-direction), *b*(dimension of y-direction). Approximated to $\sigma_{xz} = \sigma_{yz} = \sigma_{zz} = 0$; while plane strain approximation deals with long prismatic bodies, such as pressing a pipe. Approximation: $\varepsilon_{xz} = \varepsilon_{yz} = \varepsilon_{zz} = 0$.

The general form of stress, without any approximation, is:

$$\begin{aligned} \sigma_{zx} &= \frac{E}{1+\nu}\varepsilon_{zx}, \sigma_{zy} = \frac{E}{1+\nu}\varepsilon_{zy} \\ \sigma_{zz} &= \frac{E}{(1+\nu)(1-2\upsilon)}[(1-\upsilon)\varepsilon_{zz} + \upsilon(\varepsilon_{xx} + \varepsilon_{yy})] \end{aligned} \tag{5.5}$$

Equating these stress components to zero, according to plane stress definition, and by using Eq. (5.2), we obtain:

$$\begin{aligned} \varepsilon_{zx} &= \frac{1}{2}\left(\frac{\partial u_z}{\partial x} + \frac{\partial u_x}{\partial z} + \frac{\partial u_y}{\partial x}\frac{\partial u_y}{\partial z}\right) = 0 \\ \varepsilon_{zy} &= \frac{1}{2}\left(\frac{\partial u_z}{\partial y} + \frac{\partial u_y}{\partial z} + \frac{\partial u_x}{\partial y}\frac{\partial u_x}{\partial z}\right) = 0 \\ \varepsilon_{zz} &= -\frac{\upsilon}{1-\upsilon}(\varepsilon_{xx} + \varepsilon_{yy}) \end{aligned} \tag{5.6}$$

Since $\frac{\partial u_x}{\partial y} = \frac{\partial u_y}{\partial x} = 0$, Eq. (5.6) can be simplified as

$$\frac{\partial u_z}{\partial x} + \frac{\partial u_x}{\partial z} = 0, \frac{\partial u_z}{\partial y} + \frac{\partial u_y}{\partial z} = 0, \varepsilon_{zz} = -\frac{\upsilon}{1-\upsilon}(\varepsilon_{xx} + \varepsilon_{yy}) \tag{5.7}$$

Replacing u_z by $\zeta(x,y)$,

$$\begin{aligned} \partial u_x / \partial z &= -\partial \zeta / \partial x \\ \partial u_y / \partial z &= -\partial \zeta / \partial y \end{aligned} \tag{5.8}$$

Integrate Eq.(5.8) and by using u_x=0, and u_y=0 for z=0, the displacement field in x and y direction are:

$$u_x = -z\partial \zeta / \partial x, u_y = -z\partial \zeta / \partial y \tag{5.9}$$

The strain can be obtained by replacing the displacement field into Eq. (5.2),

$$\begin{aligned} \varepsilon_{xx} &= 1/2\left[2\partial u_x / \partial x + \left[\partial \zeta / \partial x\right]^2 \right] \approx \partial u_x / \partial x = -z\partial^2 \zeta / \partial x^2 \\ \varepsilon_{yy} &= 1/2\left[2\partial u_y / \partial y + \left[\partial \zeta / \partial y\right]^2 \right] \approx \partial u_y / \partial y = -z\partial^2 \zeta / \partial y^2 \\ \varepsilon_{xy} &= -z\partial^2 \zeta / \partial x \partial y \\ \varepsilon_{xz} &= \varepsilon_{yz} = 0 \\ \varepsilon_{zz} &= [\upsilon / (1-\upsilon)] z(\partial^2 \zeta / \partial x^2 + \partial^2 \zeta / \partial y^2) \end{aligned} \tag{5.10}$$

Eq. (5.10) gives the same expression as Eq. (5.4), where uniaxial stress condition is assumed and also gives shear strain. Since the general form of strain energy is

$$U_{strain} = \frac{E}{2(1+\upsilon)} \left(\sum \varepsilon_{ik}{}^2 + \frac{\upsilon}{1-\upsilon} \sum \varepsilon_{ll} \sum \varepsilon_{mm} \right) \tag{5.11}$$

by inserting Eq. (5.10) into Eq. (5.11), and general term of strain energy in the form of deformation can be written as Eq. (5.12):

$$U_{strain} = \iiint z^2 \frac{E}{1+\upsilon}\left[\frac{1}{2(1-\upsilon)}\left(\frac{\partial^2\zeta}{\partial x^2}+\frac{\partial^2\zeta}{\partial y^2}\right)^2+\left(\frac{\partial^2\zeta}{\partial x\partial y}\right)^2-\frac{\partial^2\zeta}{\partial x^2}\frac{\partial^2\zeta}{\partial y^2}\right]$$
$$= \frac{Eh^3}{24(1-\upsilon^2)}\iint\left[\left(\frac{\partial^2\zeta}{\partial x^2}+\frac{\partial^2\zeta}{\partial y^2}\right)^2+2(1-\upsilon)\left[\left(\frac{\partial^2\zeta}{\partial x\partial y}\right)^2-\frac{\partial^2\zeta}{\partial x^2}\frac{\partial^2\zeta}{\partial y^2}\right]\right]dxdy \quad (5.12)$$

Even though Eq. (5.12) for thin plate bending gives more general expression for strain and strain energy, it is still based on several approximations:

1. Plane stress approximation in obtaining Eq.(5.6). This is reasonable since in z-direction, the plate is only constrained at the boundary, which is considerably small in xy plane.
2. $\frac{\partial u_x}{\partial y}=\frac{\partial u_y}{\partial x}=0$ in obtaining Eq. (5.7) .
3. u_x=0, and u_y=0 for z=0 in obtaining Eq. (5.9), i.e., in-plane displacement is zero in the neutral plane (middle plane in z-direction). Also, $\left[\partial\zeta/\partial x\right]^2$ is assumed to be zero in Eq. (5.10), which can not be true. Therefore, the strain is modified by considering in-plane displacement induced strain:

$$\begin{aligned}
\varepsilon_{xx} &= -z\partial^2\zeta/\partial x^2+1/2\left[\partial\zeta/\partial x\right]^2\\
\varepsilon_{yy} &= -z\partial^2\zeta/\partial y^2+1/2\left[\partial\zeta/\partial y\right]^2\\
\varepsilon_{xy} &= -z\partial^2\zeta/\partial x\partial y\\
\varepsilon_{xz} &= \varepsilon_{yz}=0\\
\varepsilon_{zz} &= [\upsilon/(1-\upsilon)]\{z(\partial^2\zeta/\partial x^2+\partial^2\zeta/\partial y^2)-1/2\left[\partial\zeta/\partial x\right]^2-1/2\left[\partial\zeta/\partial y\right]^2\}
\end{aligned} \quad , \quad (5.13)$$

where u_x and u_y are considered not to be a function of y. The above argument is to determine whether $\left[\partial\zeta/\partial x\right]^2$ (strain due to stretching or compressing) or $-z\partial^2\zeta/\partial x^2$ (strain due to bending) is dominant. Take undulation of $\zeta = A\sin(kx)$ for example, $\left[\partial\zeta/\partial x\right]^2 = A^2k^2\cos^2(kx)$, and $-z\partial^2\zeta/\partial x^2 = zAk^2\sin(kx)$. Note that the relative amplitude of these two terms is A^2 and hA, or simply A and h. This means that if undulation is very small, i.e., $A<<h$, Landau's approximation is valid. However, in considering ultrathin film such as graphene, A can be comparable to h with h~0.7nm and A~0.7nm-30nm.

To simplify the problem, we split Eq. (5.13) into *stretching*: Eq. (5.14) and *bending*: Eq. (5.10).

$$\begin{aligned}
\varepsilon_{xx} &= \left[\partial\zeta/\partial x\right]^2 \\
\varepsilon_{yy} &= \left[\partial\zeta/\partial y\right]^2 \\
\varepsilon_{zz} &= [\upsilon/(1-\upsilon)]\{-\left[\partial\zeta/\partial x\right]^2 - \left[\partial\zeta/\partial y\right]^2\}
\end{aligned} \tag{5.14}$$

Then, the strain energy also splits into two terms: bending (Eq. (5.15)) and stretching (Eq. (5.16)).

$$\begin{aligned}
U_{bending} &= \frac{1}{2}\iiint(\sigma_{xx}\varepsilon_{xx} + \sigma_{yy}\varepsilon_{yy} + \sigma_{xy}\varepsilon_{xy})dV \\
&= \frac{B}{2}\iint\{\left(\frac{\partial^2\zeta}{\partial x^2} + \frac{\partial^2\zeta}{\partial y^2}\right)^2 + 2(1-\upsilon)\left[\left(\frac{\partial^2\zeta}{\partial x\partial y}\right)^2 - \frac{\partial^2\zeta}{\partial x^2}\frac{\partial^2\zeta}{\partial y^2}\right]\}dxdy
\end{aligned} \tag{5.15}$$

where the *bending modulus* is $B=Eh^3/12(1-\nu^2)$.

$$U_{streching} = h\iint [T_x \varepsilon_{xx} + T_y \varepsilon_{yy}]dxdy \tag{5.16}$$

The reason why in Eq. (5.16) there is no term like $1/2\sigma\varepsilon$ is that T_x is considered to be a constant, instead of depending on ε_{xx}, where the stress-strain diagram is triangle-like shape following Hooke's law $(\sigma=E\varepsilon)$. This is more like work= force*displacement.

5.3 Uniaxial compression of thin film

Under uniaxial compression, from Eq. (5.15), since ζ is only a function of x, the direction in which force is applied, the total energy becomes $U_{total} = U_{bending} + U_{streching} = B/2\int_A (\partial^2\zeta/\partial x^2)^2 dA + Eh/2\int_A \varepsilon_{x0}(\partial\zeta/\partial x)^2 dA$, where strain relaxation due to deformation ($\left[\partial\zeta/\partial x\right]^2$) is considered negligible to initial strain ε_{x0}. The above form of total energy is similar to Zang's results in Ref. [19].

The variation (definition shown below) of the U_{total} becomes:

$$\delta U_{total} = \int \{[B(\partial^4\zeta/\partial x^4) - hE\varepsilon_{x0}(\partial^2\zeta/\partial x^2)]d\zeta\}dA \tag{5.17}$$

Variation method in deriving Eq. (5.17) is described in detail:

$$\delta[\frac{1}{2}(\partial^2\zeta/\partial x^2)^2] = \zeta''\delta(\zeta'') = \left(\frac{d\zeta'}{dx}\right)\frac{d(\delta\zeta')}{dx} = \frac{d}{dx}\left(\frac{d\zeta'}{dx}\delta\zeta'\right) - \frac{d^3\zeta}{dx^3}\delta\zeta'$$
$$= \frac{d}{dx}\left(\frac{d\zeta'}{dx}\delta\zeta'\right) - \frac{d}{dx}\left(\frac{d^3\zeta}{dx^3}\delta\zeta'\right) + \frac{d^4\zeta}{dx^4}\delta\zeta$$

, where the first two terms can be integrated and canceled out at boundary.

$$\delta[\frac{1}{2}(\partial\zeta/\partial x)^2] = (\partial\zeta/\partial x)\delta(\partial\zeta/\partial x) = \left(\frac{d\zeta}{dx}\right)\frac{d(\delta\zeta)}{dx} = \frac{d}{dx}\left(\frac{d\zeta}{dx}\delta\zeta\right) - \frac{d^2\zeta}{dx^2}\delta\zeta ,$$

where the first term can be integrated and canceled out at boundary.

Since variation of $\delta U_{total}=0$ for any $\delta\zeta$, $B(\partial^4\zeta/\partial x^4) - hE\varepsilon_{x0}(\partial^2\zeta/\partial x^2) = 0$, with boundary condition of $\partial^2\zeta/\partial x^2\big|_{x=0,x=L} = 0$ (no bending momentum).

Therefore $\zeta(x) = \frac{c}{(m\pi/L)^2}\sin\left[\frac{m\pi}{L}x\right]$, m=1 when structure is supported at two ends of boundary (x=0, and x=L).

$$U_{total} = w[\frac{B}{2}\int c^2\sin^2(kx)dx + \frac{hE}{2}\varepsilon_{x0}\int\frac{c^2}{k^2}\cos^2(kx)dx]$$
$$= \frac{w}{4}(Bc^2L + Eh\varepsilon_{x0}\frac{c^2L^3}{\pi^2}) \qquad (5.18)$$

$$\varepsilon_{cr} = -\frac{B\pi^2}{EhL^2} = -\frac{h^2\pi^2}{12(1-\upsilon^2)L^2} \qquad (5.19)$$

To determine if the film is unstable against undulation, from Eq. (5.18) we see that

1) If $\varepsilon_{x0}=0$, i.e., no force applied to the film, c should be zero to minimize the strain energy. Therefore, no buckling happens.

2) If $\varepsilon_{x0}>0$ (tension), c should be zero to minimize the strain energy, so no buckling.

3) $\varepsilon_{x0}<0$ (compression):

3-i) If $\varepsilon_{x0}>\varepsilon_{cr}$, $c=0$ to minimize the strain energy. No buckling.

3-ii) If $\varepsilon_{x0}\leq\varepsilon_{cr}$, $c\neq0$ to minimize the strain energy. This is the condition for buckling, and ε_{cr} is the critical strain for buckling.

To further understand the buckling phenomenon, as can be seen from Eq. (5.18), bending energy is always increased due to deformation, no matter the structure is stretched or compressed; stretching energy, however, can be decreased due to deformation as long as ε_{x0} has a negative value, i.e., buckling happens only if the structure is compressed. Therefore, the competition between bending energy and tension energy results in the critical compressive strain for buckling as discussed above.

5.4 Uniaxial stretching of thin film

Under stretching along x-direction, as shown in Fig. 5.4 (a), the strain along y-direction can be written as

$$\varepsilon_{yy} = 1/E(\sigma_{yy} - \upsilon(\sigma_{xx} + \sigma_{zz})) \tag{5.20}$$

In this case, if the length of the film is large, we only need to consider the middle region, where the dominant stress is in x-direction, i.e., $\sigma_{yy}=0$. Here we neglect the boundary part, where the σ_{yy} can be comparable to σ_{xx}. Therefore Eq. (5.20) becomes:

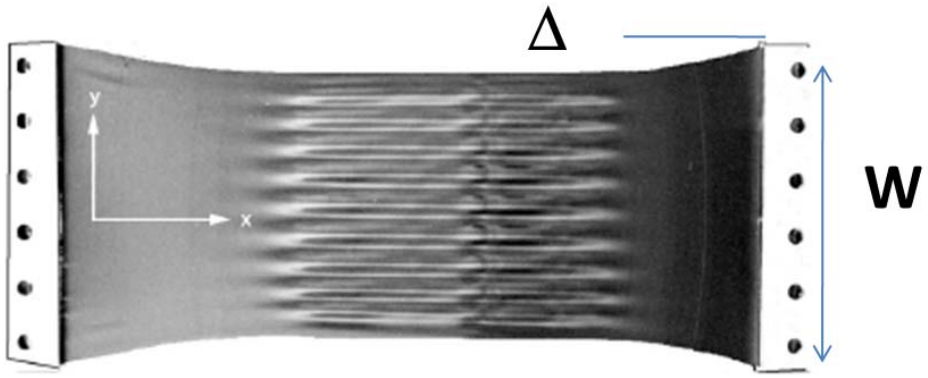

(a)

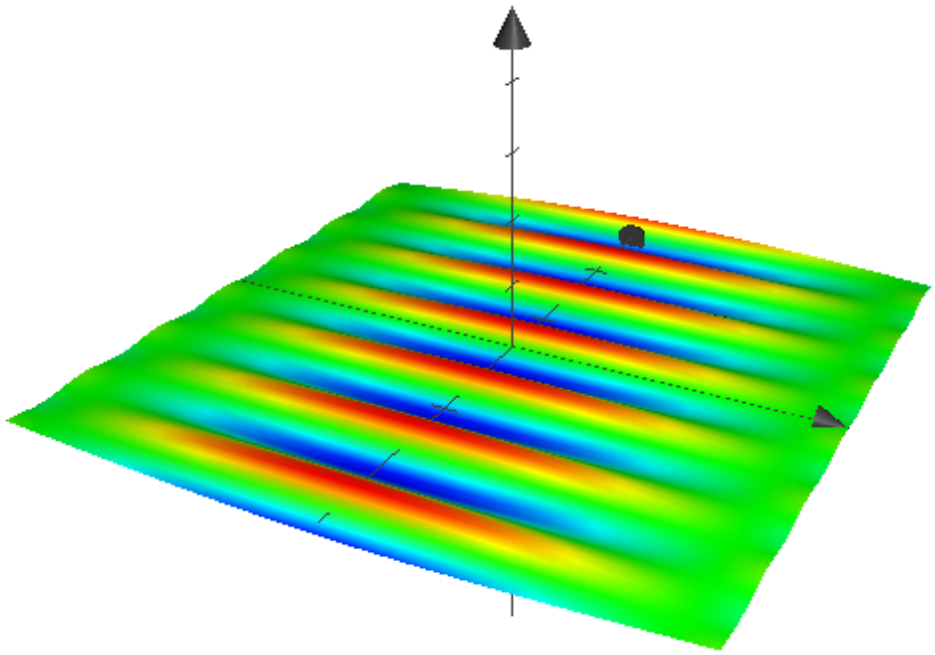

(b)

Fig. 5.4 Uniaxial stretching of thin film. (a) Experimental uniaxial stretching of thin film [20]. (b) Schematic plot of Eq. (23), where height profile is indicated in red (z_max) to blue (z_min).

$$\varepsilon_{yy} = -\upsilon\sigma_{xx} / E = -\upsilon\varepsilon_{xx}, \tag{5.21}$$

Because of this strain in y direction due to the Poisson effect, the film ripples. The variation of total energy in this case, which is different from the uniaxial compression case, has an additional term, stretching in y direction:

$$\begin{aligned}\delta U_{total} = [W\int B(\partial^4\zeta / \partial y^4)d\zeta - hW\int E\varepsilon_{x0}(\partial^2\zeta / \partial x^2)d\zeta \\ +hL\int \upsilon\varepsilon_{x0}(\partial^2\zeta / \partial y^2)d\zeta]\end{aligned}, \tag{5.22}$$

where W is the width, and L is the length, in which direction tensile stress is applied. Hence, the following equation must be satisfied:

$$B(\partial^4\zeta / \partial y^4) - hE\varepsilon_{x0}(\partial^2\zeta / \partial x^2) + (L/W)E\upsilon\varepsilon_{x0}(\partial^2\zeta / \partial y^2) = 0 \tag{5.23}$$

Because no constraint is applied in y direction in the middle region, there can be multiple wave modes in y direction. On the other hand, since the two ends of film are constrained in x direction, it can only have one mode along this direction. Therefore, the deformation can be described as

$$\zeta(x, y) = a\sin(ky)\cos(\pi x / L) \tag{5.24}$$

Fig. 5.4 (b) shows the deformation according to Eq. (5.24), which is consistent with the experimental observation as shown in Fig. 5.4 (a).

$$U_{total} = \frac{B}{2}\int_A (\frac{\partial^2 \zeta}{\partial y^2})^2 dxdy + \frac{Eh}{2}\int \varepsilon_{x0}(\frac{\partial \zeta}{\partial x})^2 dxdy - \frac{Eh}{2}\upsilon\int \varepsilon_{x0}(\frac{\partial \zeta}{\partial y})^2 dxdy \qquad (5.25)$$

Taking Eq. (5.24) into Eq. (5.25),

$$U_{total} = \frac{LWa^2}{8}(Bk^4 + Eh(\frac{\pi}{L})^2 \varepsilon_{x0} - Ehk^2 \nu \varepsilon_{x0}) \qquad (5.26)$$

Similar to Eq. (5.18), which is the compression case, for undulation to happen, the following must be satisfied:

$$Bk^4 + Eh(\frac{\pi}{L})^2 \varepsilon_{x0} - Ehk^2 \nu \varepsilon_{x0} \le 0 \qquad (5.27)$$

Solving Eq. (5.27), and taking $k=n(\pi/W)$,

$$\varepsilon_{x0} \ge \varepsilon_{cr} = \frac{Bk^4}{Eh\nu k^2 - Eh(\pi / L)^2} = \frac{h^2\pi^2}{12(1-\nu^2)} \frac{n^4}{W^2[n^2 - (W/L)^2]} \qquad (5.28)$$

Comparing Eq. (5.28) (uniaxial tension) with Eq. (5.19) (uniaxial compression), we can see that if the length L, along which the uniaxial tension is applied, is infinite long, the buckling will only occur in the width direction, with Eq. (5.28) having the same form as Eq. (5.19).

5.5 MD simulations of mechanical instability in graphene

The analyses in Section 5 shows that there should be a maximum asymmetry in the strain induced instability of tension versus compression in graphene, because graphene is the thinnest possible film with only one atomic layer thick. Especially, the critical compressive strain for buckling in graphene can be very small. Taking the thickness to be 0.7 Å with a Poisson's ratio of 0.34 [21, 22], the single layer graphene usually has a thickness (~nm) much smaller than its length (~μm). Consequently, it will buckle under a very small amount of compression, which can be easily caused by thermal fluctuation induced compression alone. In other words, unless graphene layers are biaxially stretched, they cannot exist in flat 2D shape. As derived above, the critical compressive strain for one mode of buckling can be written as Eq. (5.19). Similarly, under fluctuation and small perturbation, multiple modes of rippling can be formed and the critical strain can be written as:

$$\varepsilon_{cr} = \frac{Bn^2\pi^2}{EhL^2} = -\frac{h^2\pi^2 n^2}{12(1-\upsilon^2)L^2} \tag{5.29}$$

Using the known graphene parameters, Eq. (5.29) is plotted in Fig. 5.5. It can be seen that for a given L, number of modes increases with ε, and the period of the rippling pattern can be tuned by the magnitude of the compressive strain and the length of graphene [23]. We also calculate the critical strain for buckling by molecular static relaxation at T=0 K, and the calculation details are given in Section 2.3. We used Tersoff potential [24] to determine the equilibrium state of graphene. The equilibrium C-C bond length of planar graphene is calculated to be 1.46 Å. Young's modulus is calculated to be 1.24 TPa, which is comparable to literature results using similar potential [25].

To study buckling of graphene under uniaxial compression, we introduce an initial perturbation in out-of-plane direction and apply uniaxial strain by changing the periodic box size. Fig. 5.6 shows the strain energy versus strain for the flat (without out-of-plane perturbation) and undulated (with out-of-plane perturbation) graphene. Under small strains, the two curves merge together. However, if the absolute value of strain exceeds certain value, the undulated structure with initial out-of-plane perturbation is energetically more favorable. We define this strain as the critical strain for buckling.

Next, we analyze critical strain for different dimensions of graphene to see the dependence of the critical strain on the length of graphene under compression. Figure 5.7 shows the critical strain versus L^{-2} for uniaxial compression of graphene ribbons along the zigzag and armchair directions. A linear relationship between the critical strain and L^{-2} is found for both cases, and this relationship is not dependent on the direction of the applied compression. The critical strain versus L^{-2}, as described in Eq. (5.29), with n=2, Poisson's ratio ν=0.19 [26] and the thickness of single layer graphene t=0.66 Å [26], is

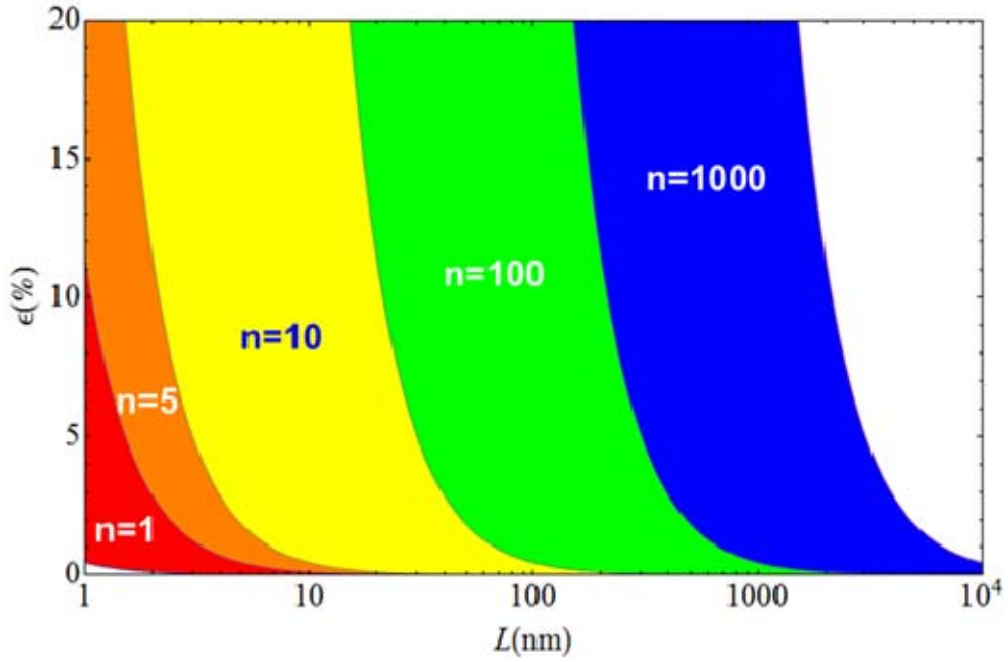

Fig. 5.5 Phase diagram showing the number of ripple periods (n) formed as a function of the graphene length (L) and the applied compressive strain (ε). Boundary lines mark the critical strain (ε_{cr}) in Eq. (5.29). [23]

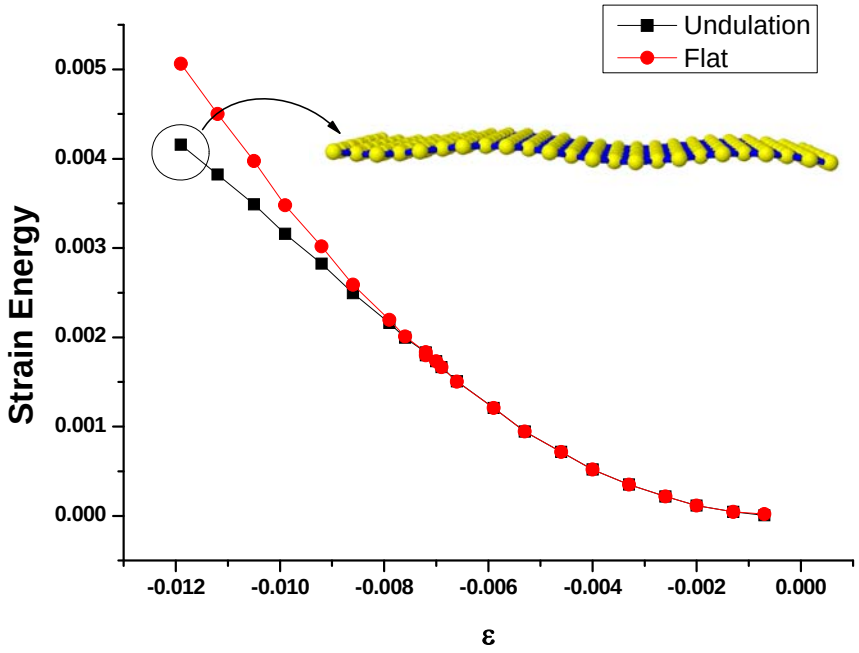

Fig. 5.6 Strain energy versus strain for graphene with dimension of LX=15.18 Å and LY=13.14 Å, uniaxial strain is applied in x-direction.

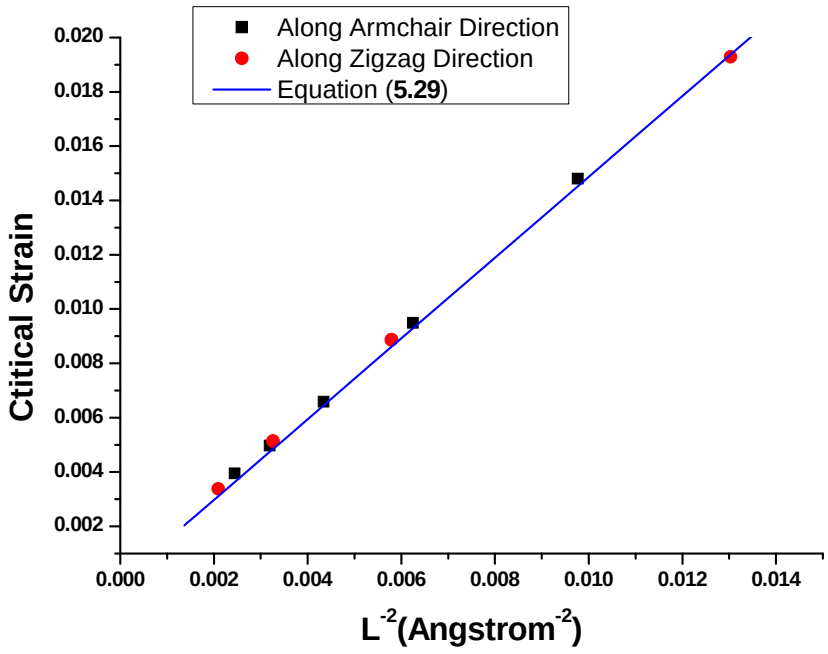

Fig. 5.7 Critical strain for uniaxial compression versus L^{-2}

also plotted in this figure and we see that the derived equation agrees very well with the simulation results.

A similar approach is used in calculating buckling of graphene under biaxial compression. If a rectangular material is biaxially compressed with same amount of strain, the longer side will buckle first and the shorter side will never buckle since it will be energetically unfavorable. Therefore, to study the biaxial buckling problem, we need to choose a square or nearly square geometry. Due to the geometric nature of graphene, it is impossible to have a graphene ribbon with identical length along zigzag edge and armchair edge. Hence in studying biaxial compressing, we use a geometry that is close to a square. Graphene ribbon with the dimension of 12.65 Å (with zigzag edge) by 13.14 Å (with armchair edge), 25.30 Å by 26.28 Å and 37.95 Å by 39.42 Å are biaxially compressed and the critical strain is shown in Fig. 5.7. In plotting this figure, length is averaged and the critical strain is compared with uniaxial compression results using Eq. (5.29) discussed in previous section. The analytical solution of this problem is described as [27]:

$$\varepsilon_{x,bi} = \frac{\pi^2 t^2 n^2}{12(1-\upsilon^2)L'^2} \tag{5.30}$$

where $L'^{(-2)} = \left(L_x^{(-2)} + L_y^{(-2)}\right)/2$ with $Lx \approx Ly$, and with the undulation profile of $\zeta = c\sin(\frac{n\pi}{L_x}x)\sin(\frac{n\pi}{L_y}y)$. We can see Eq. (5.30) and Eq. (5.29) have the same form, and it is confirmed by simulation results plotted in Fig. 5.8.

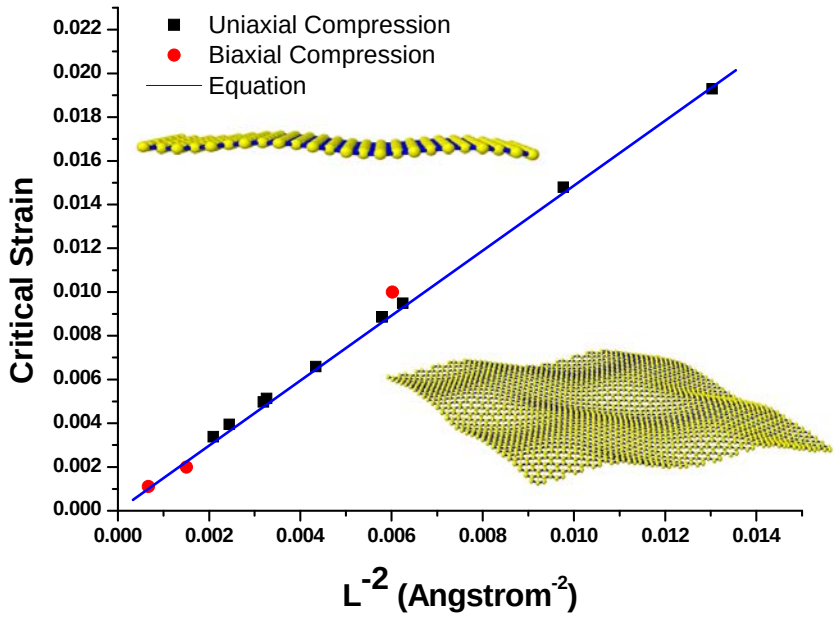

Fig. 5.8 Critical strain for biaxial compressing versus L^{-2}, where insets indicate buckling under uniaxial compression (top) and biaxial compression (bottom)

Uniaxial stretching along armchair and zigzag directions is also simulated and energy dependence on strain is plotted in Fig. 5.9. From this figure, we can see that after strain reaches a critical value, energy becomes constant, indicating fracture formation in graphene. For uniaxial stretching along armchair direction, the strain where graphene breaks is 16.7%, and for stretching along zigzag direction, the value is 22.7%. However, since all the bonds in graphene are uniformly stretched and periodic boundary condition is used in our MD simulation, this value can be larger than it should be. Therefore, we can also use energy comparison to determine the reasonable values of critical strain, as can been seen from the intersection in Fig. 5.9. The critical strain for stretching along armchair direction is 10% and along zigzag direction is 12.5%. This result is smaller than the molecular mechanics result (28.2%, [28]) and the experimental result (25%, [2]).

We also notice that the energy after breaking of graphene does not go back to zero due to the energy cost of creating two fracture edges, i.e., edge energies (in analogy to interface energies for creating two surfaces). Therefore, we calculate the edge energies to be 0.2926 eV/atom (1.07 eV/Å) for armchair edge and 0.3863 eV/atom (0.92 eV/Å) for zigzag edge. This result is comparable to molecular dynamics results using reactive empirical bond-order potential [29], but different from first-principles results [30-31]. This is due to the intrinsic inaccuracy of empirical potential, neglecting electronic structure.

One effective approach to apply strain to graphene is by heteroepitaxial growth of graphene on a substrate. A recent experiment [15] showed formation of graphene bubbles as graphene is grown on Pt (111) surface, as shown in Fig. 5.10 [15]. It was suggested [15] that graphene bubbles are under large “tensional” strain with a substantial (5-10%)

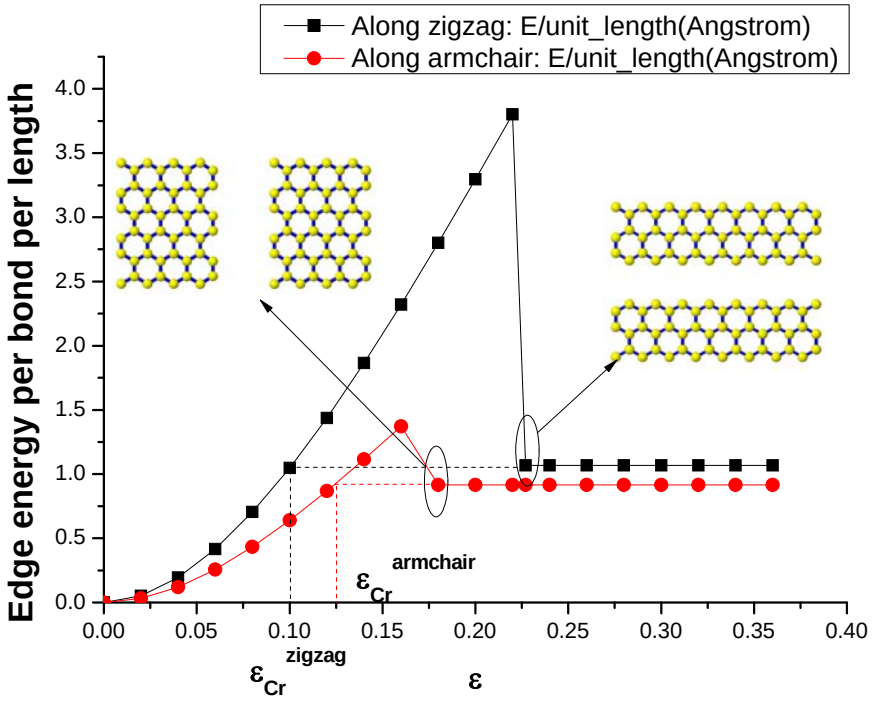

Fig. 5.9 Energy vs. strain for uniaxial stretching along armchair and zigzag directions, where insets indicate breaking under uniaxial compression applied along zigzag direction (left) and armchair direction (right)

change in bond length in order to induce a pseudo-magnetic field responsible for the STM measured electronic level splitting. However, the exact strain distribution and the amount of strain inside graphene nanobubbles are not truly known, only speculated. Here, using MD simulations, we directly map out the strain field inside the graphene nanobubble.

Due to the honeycomb geometry of graphene, we use a triangle shape, which can be repeated by using periodic boundary condition, to represent the whole graphene sheet. Another triangle shape is defined within the big triangle, as shown in Fig. 5.10 (a), and the atoms in this inner triangle are allowed to move in all three directions, i.e., no degree of freedom (d.o.f) is fixed. The atoms in between the two triangles, representing atoms attached to substrate, have two scenarios. One is to fix their out-of-plane z-component but allow relaxation of their in-plane d.o.f, which means incoherent interfacial bonding between graphene and substrate. Another scenario is to fix all their d.o.f subject to the predefined amount of strain, which means a coherent interface.

Figure 5.11 and 5.12 show the relaxed graphene bubble with 10% triaxial strain for the incoherent and coherence interface, respectively. Figure 5.13 and 5.14 show the corresponding strain distribution contour plot, respectively. Comparing Fig. 5.13 with Fig. 5.14, we can see that the most relaxed area (~5% residual strain) for the case of incoherent interface is at the corners of the inner triangle, while the most relaxed area (0.3% residual strain) for the case of coherent interface is at the ridges of the pyramid. This is because for the coherent case, the atoms outside the inner triangle are not allowed to relax, while for the incoherent case, relaxation is realized by all the atoms including atoms bonded to the substrate.

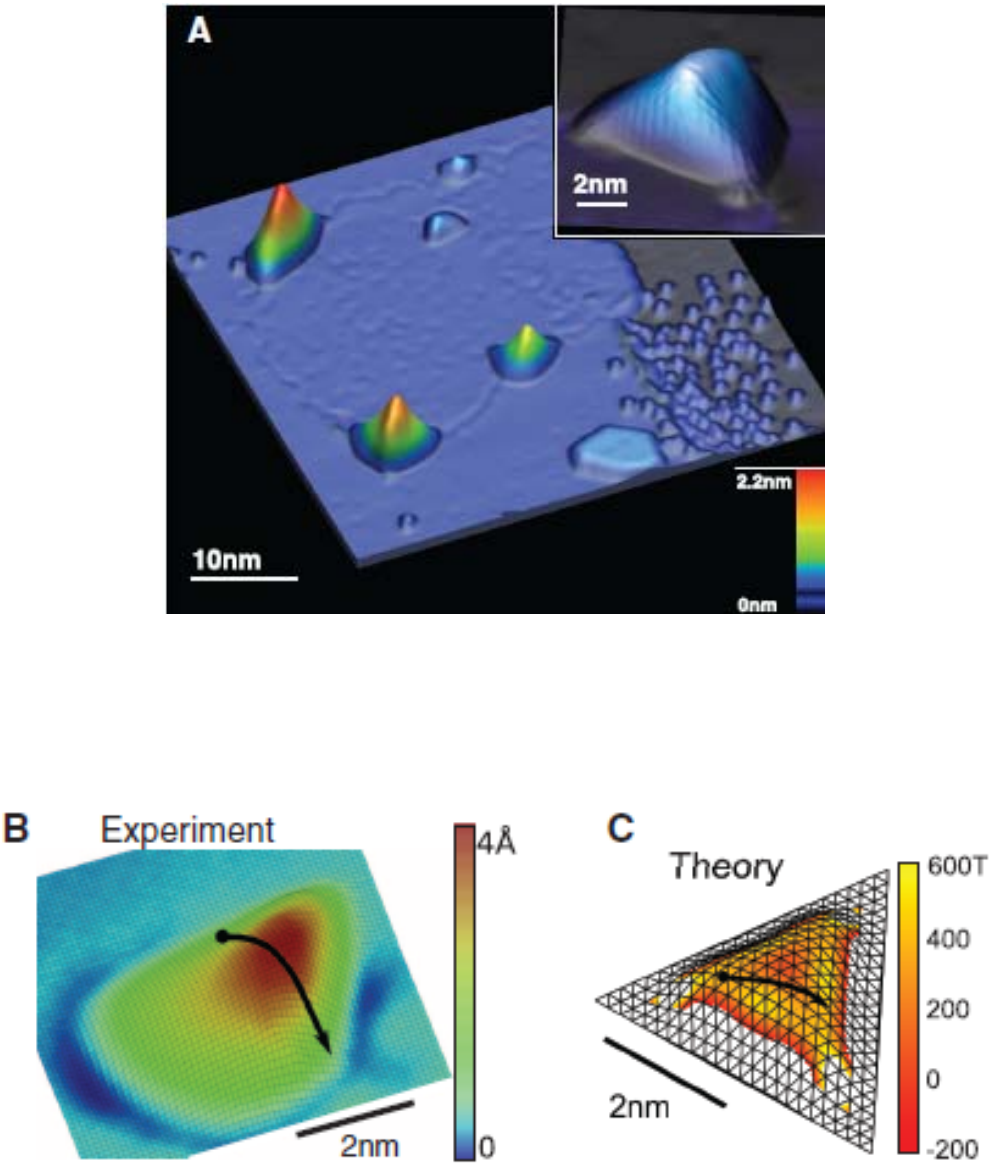

Fig. 5.10 Experimental observed graphene nanobubble (a) STM image of graphene monolayer patch on Pt (111), with inset showing high-resolution image of a graphene nanobubble showing distorted honeycomb lattice; (b) STM topography of graphene nanobubble; (c) Topography of theoretically simulated graphene nanobubble. [32]

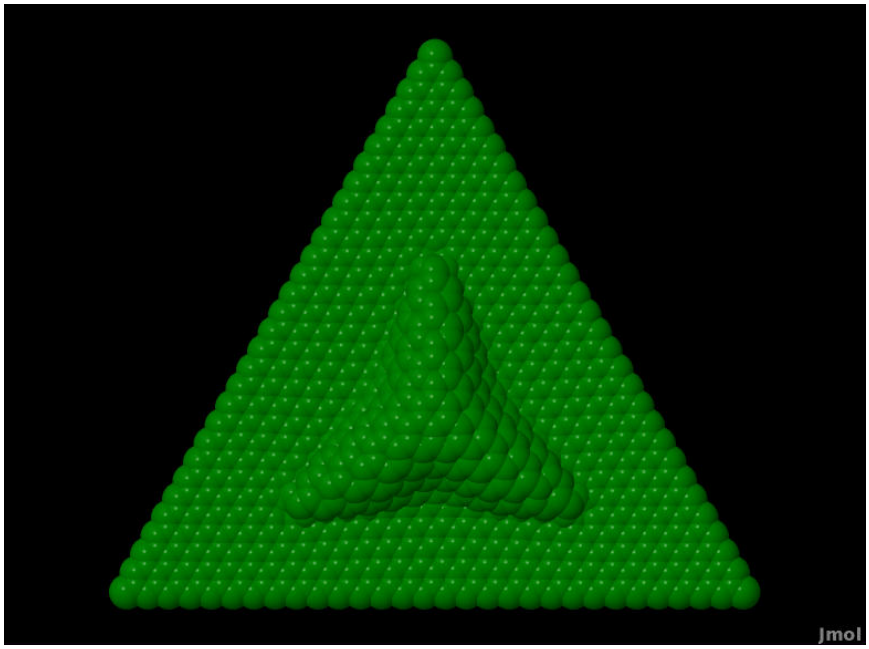

(a)

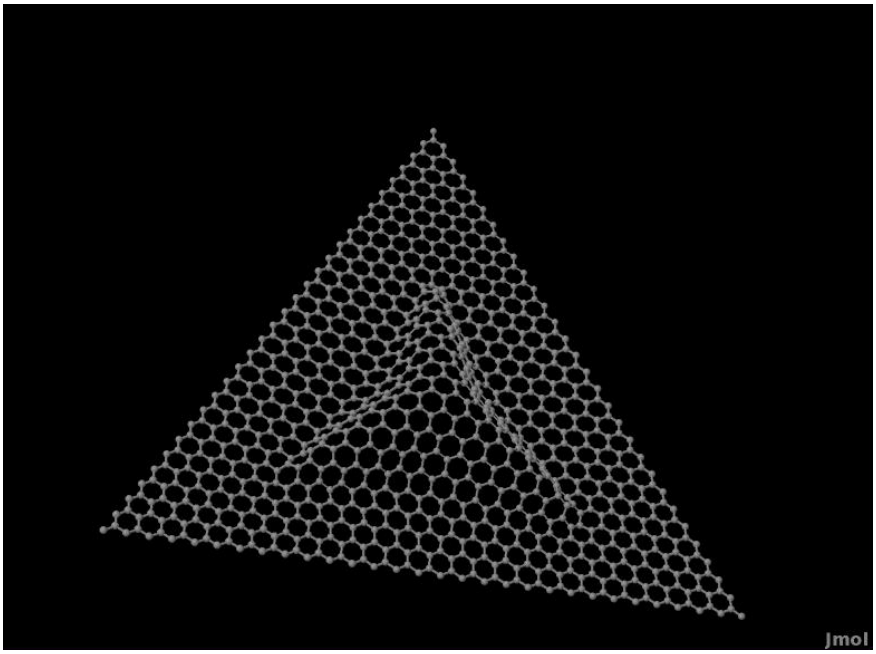

(b)

Fig. 5.11 Relaxed graphene nanobubble with 10% strain for imperfect bonding between graphene and substrate.

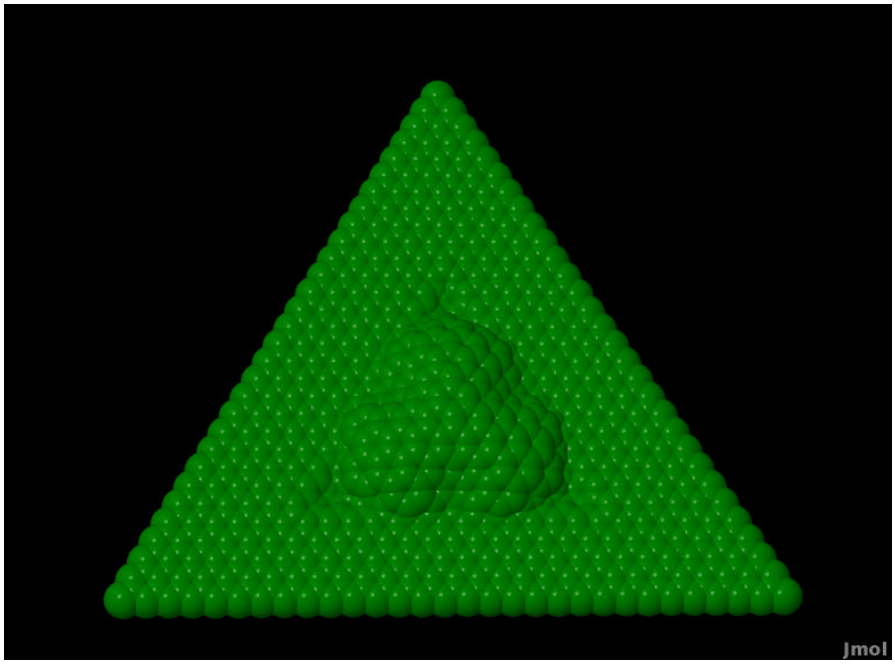

(a)

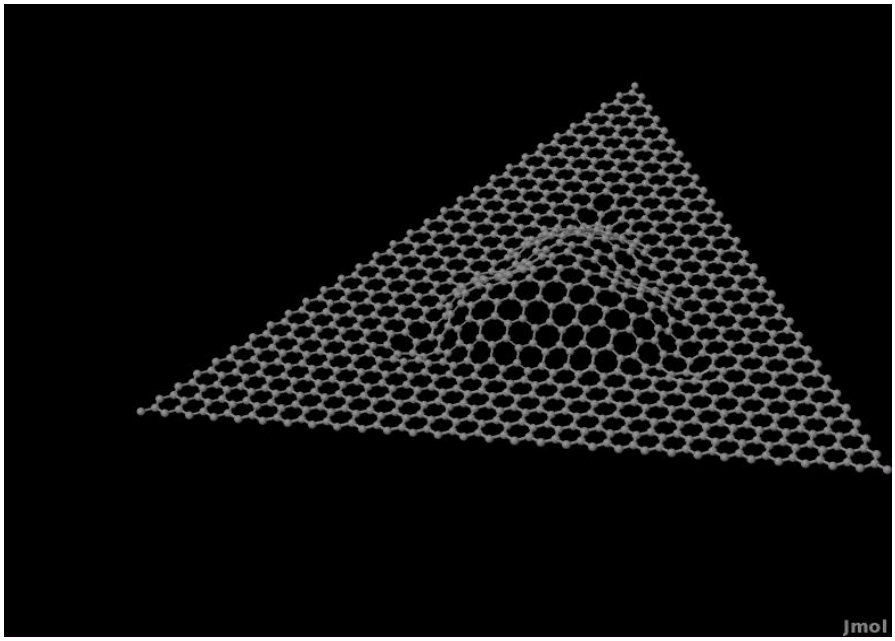

(b)

Fig. 5.12 Relaxed graphene nanobubble with 10% strain for perfect bonding between graphene and substrate.

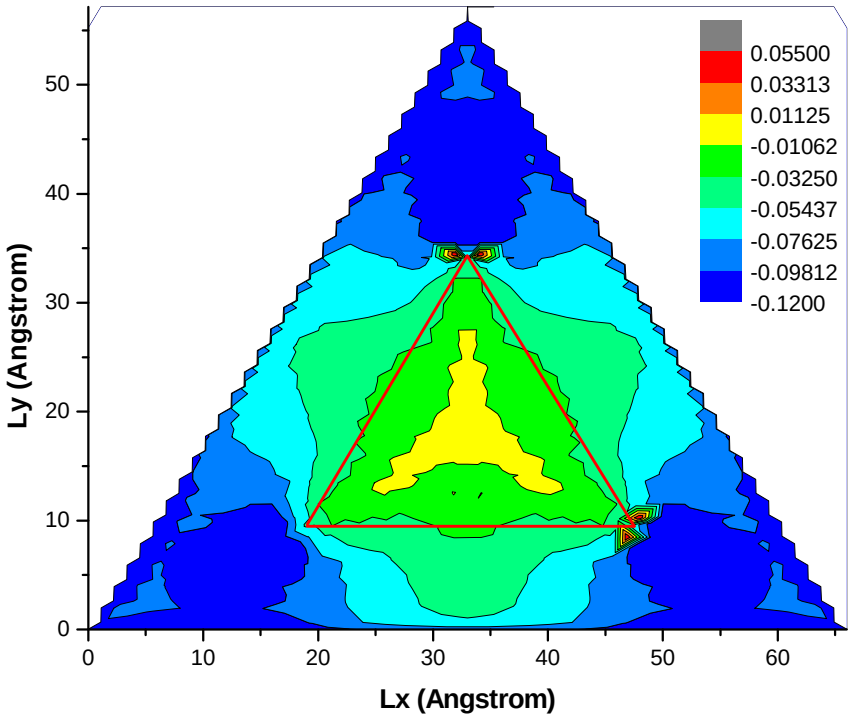

Fig. 5.13 Strain contour plot for graphene bubble imperfectly bonded to the substrate.

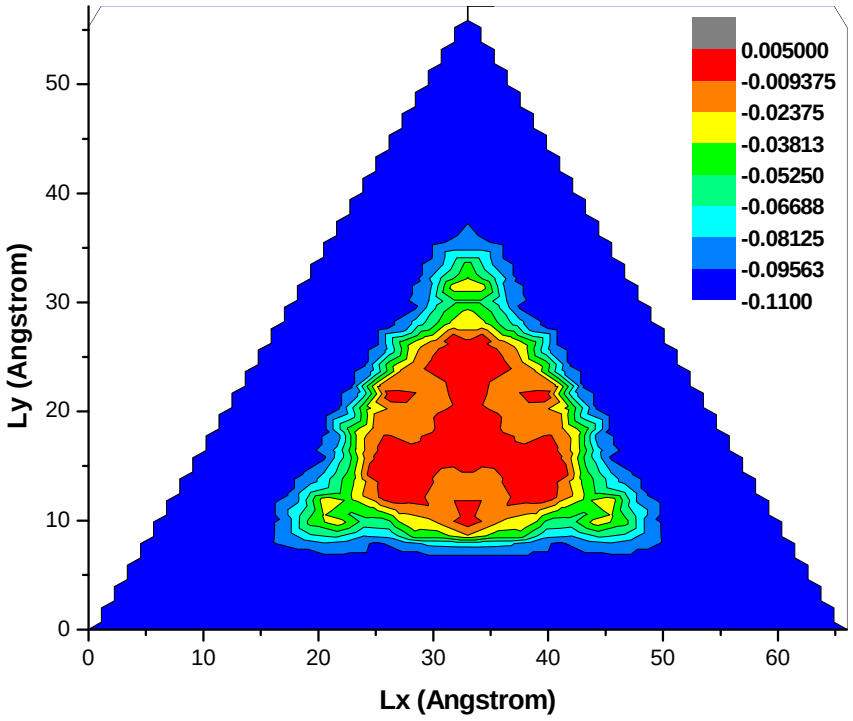

Fig. 5.14 Strain contour plot for graphene bubble perfectly bonded to the substrate.

5.6 Summary

We have applied continuum mechanics and variational perturbation theory to analyze the mechanical instability of graphene, the thinnest 2D film, and derive the critical strain for uniaxial and biaxial compression versus tension, which exhibits a maximum asymmetry. We performed molecular statics calculations at T=0 K to obtain the strain energies associated with buckling and fracture formation of graphene. We found that the critical compressive strain for the buckling instability scales with L^{-2}, where L is the length of graphene, which is in good agreement with the continuum mechanics theory. By fitting the MD results with analytical solution, the thickness of single layer graphene is derived to be ~0.66 Å. The critical tensile strain for fracture is found to be dependent on the load directions, which are 10% and 12.5% for the fracture along the armchair and zigzag direction, respectively. The edge energies for armchair and zigzag edges are calculated to be 1.07 eV/Å and 0.92 eV/Å, respectively. We also performed MD simulations for the formation of graphene nanobubble induced by misfit strain when graphene is grown on a substrate. We analyzed the atomic structure and strain distribution inside the graphene nanobubbles under two extreme conditions: one with the inherent graphene-substrate interface and the other with the coherent interface. We find the strain relaxation mechanism is different for the two cases, and the strain inside the graphene nanobubble has a maximum value of 5% for the incoherent interface case at the corners of pyramid and 0.3% for the coherent interface case at the top of pyramid.

5.7 References

1. J. S. Bunch, A. M. van der Zande, S. S. Verbridge, I. W. Frank, D. M. Tanenbaum, J. M. Parpia, H. G. Craighead, and P. L. McEuen, Science 315, 490 (2007)

2. C. Lee , X. D. Wei, J. W. Kysar, and J. Hone, Science 321, 385 (2008).

3. T. J. Booth, P. Blake, R. R. Nair, D. Jiang, E. W. Hill, U. Bangert, A. Bleloch, M. Gass, K. S. Novoselov, M. I. Katsnelson, and A. K. Geim, Nano Lett 8, 2442 (2008)

4. Y. Zhang, Y. Tan, H. L. Stormer and P. Kim, Nature 438, 201 (2005)

5. A. K. Geim and K. S. Novoselov, Nature Materials 6, 183 (2007)

6. K. S. Novoselov, A. K. Geim, S. V. Morozov, D. Jiang,Y. Zhang, S. V. Dubonos, I. V. Grigorieva, and A. A. Firsov, Science 306, 666 (2004)

7. K. S. Novoselov, D. Jiang, F. Schedin, T. J. Booth, V. V. Khotkevich, S. V. Morozov, and A. K. Geim, Proc. Natl. Acad. Sci. U.S.A. 102, 10451 (2005)

8. C. Berger, Z. Song, X. Li, X. Wu, N. Brown, C. Naud, D. Mayou, T. Li, J. Hass, A. N. Marchenkov, E. H. Conrad, P. N. First, and W. A. de Heer, Science 312, 1191 (2006)

9. X. Li, X. Wang, L. Zhang, S. Lee, and H. Dai, Science 319, 1229 (2008).

10. V. M. Pereira and A. H. Castro Neto, Phys. Rev. Lett. 103, 046801 (2009).

11. Y. Son, Marvin L. Cohen, and S. G. Louie, Phys. Rev. Lett. 97, 216803 (2006).

12. Y.Lu and J. Guo, Nano Res 3, 189 (2010).

13. M. Poetschke, C. G. Rocha, L. E. F. Foa Torres, S. Roche, and G. Cuniberti, Phys. Rev. B 81, 193404 (2010)

14. L. Sun, Q. Li, H. Ren, H. Su, Q. W. Shi, and J. Yang, J. Chem. Phys. 129, 074704 (2008).

15. N. Levy, S. A. Burke, K. L. Meaker, M. Panlasigui, A. Zettl, F. Guinea, A. H. Castro Neto, and M. F. Crommie, Science 329, 544 (2010)

16. W. Bao, F. Miao, Z. Chen, H. Zhang, W. Jang, C. Dames and C. N. Lau, Nature Nanotechnology 4, 562 (2009)

17. C. Chen, W. Bao, J. Theiss, C. Dames, C. N. Lau, and S. B. Cronin, Nano Letter 9, 4172 (2009)

18. L. D. Landau, L. P. Pitaevskii, E.M. Lifshitz, and A. M. Kosevich, *Theory of Elasticity, Third Edition* (Butterworth-Heinemann, 1986).

19. J. Zang and F. Liu, Appl. Phys. Lett. 92, 021905 (2008).

20. E. Cerda and L. Mahadevan, Phys. Rev. Lett. 90, 074302 (2003).

21. J. Zang, O. A. Palacios and F. Liu, Commun. Comput. Phys. 2, 451 (2007).

22. Z.Tu and Z. Ou-Yang, Phys. Rev. B 65, 233407 (2002).

23. Z. F. Wang, Y. Zhang, and F. Liu, Phys. Rev. B 83, 041403(R) (2011).

24. J. Tersoff, Phys. Rev. B 39, 5566 (1989).

25. Y. Jin and F. G. Yuan, Compos. Sci. Technol. 63, 1507 (2003).

26. B. I. Yakobson, C. J. Brabec, and J. Bernholc, Phys. Rev. Lett. 76, 2511 (1996).

27. S. P. Timoshenko and J. M. Gere, *Theory of Elastic Stability* (McGraw-Hill, 1961).

28. Q. Lu and R. Huang, Int. J. Applied Mechanics 1, 443 (2009).

29. Q. Lu and R. Huang, Phys. Rev. B 81, 155410 (2010).

30. P. Koskinen, S. Malola, and H. Hakkinen, Phys. Rev. Lett. 101, 115502 (2008).

31. B. Huang, M. Liu, N. Su, J. Wu, W. Duan, B. Gu, and F. Liu, Phys. Rev. Lett 102, 166404 (2009).